Numerical simulation of commercial scale autothermal chemical looping reforming and bi-reforming for syngas production

Zirui He [a, b], Juray De Wilde [a, b, *]
[a] *Université catholique de Louvain, Institute of Mechanics, Materials and Civil Engineering (iMMC), Materials & Process Engineering (IMAP), Place Sainte Barbe 2, B-1348 Louvain-la-Neuve, Belgium*
[b] *Research and Innovation Centre for Process Engineering (ReCIPE), Place Sainte Barbe 2, B-1348 Louvain-la-Neuve, Belgium*

Abstract: Autothermal Chemical Looping Reforming (a-CLR) is an emerging technology that facilitates CO_2 capture and minimizes energy losses in syngas production. The dual-fluidized bed process uses a bubbling fuel reactor (FR) and a riser air reactor (AR). A 1-D multiscale model was developed that couples fluidized bed hydrodynamics with intrinsic reaction kinetics, including catalyst deactivation by oxidation and coke formation. An a-CLR unit with a capacity equivalent to 50 conventional reformer tubes was considered to demonstrate feasibility. The effects of the catalyst activity, main operation conditions and CO_2 co-feeding on the performance were then analyzed. The results confirm a-CLR is feasible with realistic reactors dimensions and solids circulation rate. To avoid the risk of sintering and catalyst deactivation, the oxygen carrier should only be slightly oxidized in the AR. Autothermal operation then requires an oxygen-to-CH_4 feed ratio of around 1.2. The high catalyst-to-gas feed ratio in the FR and bubble-emulsion phase mass transfer limitations result in a low sensitivity of the methane conversion to the catalyst activity. A low H_2O-to-CH_4 feed ratio introduces a risk for coke formation in the bottom of the FR, but part of the feed methane is fully oxidized, producing H_2O and CO_2 in the emulsion phase and mitigating this risk. Co-feeding CO_2 with CH_4 and H_2O is seen to allow adjusting the H_2/CO-ratio of the syngas, but

---

[*] *Corresponding author: Tel. +32 10 47 8193. E-mail address: juray.dewilde@uclouvain.be*

increases the risk of coke formation. Finally, heat recovery from the flue gas and syngas from both reactors by preheating the feed gases further increases the energy efficiency.

Keywords: Chemical Looping; Syngas; Steam Methane Reforming; Bi-reforming; Autothermal reforming.

Nomenclature

Roman Symbols	*Description*	*Units*
a_v	Specific interchange area per unit reactor	$[m_{interface}^2/m_r^3]$
A_0	Orifice area of the plate	$[m_r^2]$
A_j	Preexponential factor of reaction kinetic constant and equilibrium constant considered in this work.	See Table A. 1
$\hat{A}_i$	Preexponential factor of adsorption constant	See Table A. 1
Ar	Archimedes number	[-]
B_j	Parameters for equilibrium constant of reforming and water-gas-shift reactions, $j = R5, R6, R7$ (See Table A. 1)	$[\mathrm{K}]$
C_{Ab} / C_{Ae}	Species concentration in the bubble phase and emulsion phase in the FR	$[mol_A/m_{bg}^3]$ $[mol_A/m_{eg}^3]$
C_D	Drag coefficient	[-]
C_j	Constants for calculating equilibrium constant of reforming and water-gas-shift reactions, $j = R5, R6, R7$ (See Table A. 1)	[-]
C_{Ni} / C_{NiO}	Concentration of solid species	$[mol/kg_s]$
C_g/C_g^s	Concentration of gas species in bulk gas or solids phase in the AR	$[mol_g/m_g^3]$ $[mol_g/kg_s^3]$
C_p	Specific heat of gas and solids	$[kJ/kg \cdot K]$
d_b	Bubble diameter	$[m_b]$
d_p	Particle diameter	$[m]$
d_t	Reactor diameter	$[m_r]$

$D_{eg}/\ D_{es}$	Effective axial dispersion coefficient of gas and solids	$[m_r^2/s]$
E_a	Activation energy of reactions considered in this work	$[kJ/mol]$
F_A	Species molar flow rate	$[mol_A/s]$
$\hat{F}_{O_2}/\ \hat{F}_{N_2}$	Oxygen and nitrogen molar flux in the riser	$[mol_{O_2/\ N_2}/m_r^2 \cdot s]$
$\hat{F}_{Ab}\ /\ \hat{F}_{Ae}$	Species flow rate in the bubble phase and emulsion phase in the FR	$[mol_A/m_r^2 \cdot s]$
f_b	Bubble fraction in the BFB	$[m_b^3/m_r^3]$
f_{eg}	Emulsion gas fraction in the BFB	$[m_{eg}^3/m_r^3]$
f_{es}	Solids fraction in the BFB	$[m_s^3/m_r^3]$
f_g	Gas-wall friction factor	[-]
f_s	Solids-wall friction factor	[-]
g	Acceleration of gravity	$[m/s^2]$
$G_g^{in\ AR}$	Air feed rate into the AR	$[kg_{air}/s]$
h_f	Heat transfer coefficient	$[J/m^2Ks]$
H_{FR}	Height of BFB dense zone	$[m_r]$
j_D, j_H	j-factor for mass transfer/heat transfer	[-]
k_g	Mass transfer coefficient	$[m_g^3/m_{interface}^2 \cdot s]$
k_I	Interexchange mass transfer coefficient	$[m_g^3/m_r^3 \cdot s]$
k_j	Kinetic constant of reactions simulated in this work, $j = R1 - R9$	See Table 2
K_j	Equilibrium constant of reforming and water-gas-shift reactions, $j = R5, R6, R7$	[-]
K_A	Adsorption constant, $A = O_2, CO, CH_4, H_2O, H_2$	See Table 2

L_{AR}	Length of riser	$[m_r]$
$\dot{m}_s$	Solids circulation rate, defined by fully reduced OC	$[kg_s/s]$
M_{O_2}	Molar mass of O_2	$[kg/mol]$
n_{Red}	Apparent chemical reaction order of NiO reduction reactions, Red $= R2, R3, R4$	[-]
p_A	Species partial pressure, $A = O_2, CH_4, CO, CO_2, H_2O, H_2$	$[bar]$
$p_{O_2}^s$	Oxygen partial pressure in the solids	$[bar]$
Pr	Prandtl number	[-]
r_j & r_j^{Ni}	Reaction rate of reactions simulated in this work, the superscript Ni denotes the reaction rate on fully reduced catalyst, $j = R1 - R7$	$[mol/kg_s \cdot s]$
R	Gas constant, 8.314	$[J/mol \cdot \mathrm{K}]$
R_A	Overall rate of producing species A	$[mol_A/kg_s \cdot s]$
Re	Reynolds number	[-]
Sc	Schmidt number	[-]
T, T_s	Bulk gas and solids temperature in the AR	[K]
T_{env}, T_{WGS}	Environment temperature and temperature of typical water-gas-shift reaction	[K]
T_{FR}	Temperature of the FR	[K]
T_g	Gas temperature	[K]
u_b, u_{eg}	Gas velocity in bubble phase and emulsion phase	$[m_r/s]$
u_{sg},u_{mf}	Superficial gas velocity and minimum fluidization velocity in the FR	$[m_g^3/m_r^2 \cdot s]$
u_{sp}	Mean particle velocity in the FR	$[m_r/s]$

u_{ss}	Superficial solids velocity	$[m_s^3/m_r^2 \cdot s]$
u_t	Terminal velocity	$[m_r/s]$
$x_{O_2}, x_{Ni}, x_{CH_4}$	Conversion of oxygen, Nickel and methane	[-]

Greek symbols

ε_g	Void fraction in the riser	$[m_g^3/m_r^3]$
ε_{mf}	Void fraction of minimum fluidization state in BFB	$[m_g^3/m_r^3]$
μ	Dynamic viscosity	$[Pa \cdot s]$
δ_{O_2}	Expansion per mole of O_2	[-]
ρ_g, ρ_s	Gas and solid density	$[kg/mol]$
φ_{NiO}	Deactivation function accounts for NiO in the catalyst	[-]
ΔH^r	Reaction enthalpy	$[kJ/mol]$
ΔH^a	Adsorption enthalpy, different subscript indicates different gas	$[kJ/mol]$
$\Delta F_{A,Ei}$	Excess flow from emulsion phase to bubble phase due to reactions	$[mol_A/m_r^3 \cdot s]$
Ω	Reactor cross section	$[m_r^2]$

1 Introduction

Hydrogen as well as syngas (a mixture of CO and H_2) are key industrial intermediates widely used in methanol production, ammonia synthesis and the petroleum industry [1,2]. There are three commercial routes converting natural gas into syngas/hydrogen, steam methane reforming (SMR), partial oxidation (POX) and autothermal reforming (ATR). SMR is conducted in a large number of tubular reactors suspended in a furnace and produces about 75% of world’s total hydrogen, but emits about 7 kg of CO_2 per kg H_2 [3] and as such accounts for around 3% of the worldwide CO_2 emissions. Alternative processes for syngas production do not need heat supply from a furnace and prevent the related CO_2 emissions and loss in energy efficiency. The non-catalytic or catalytic partial oxidation of methane (POM / CPOM) convert methane with oxygen or air to H_2 and CO. Operation at high temperature and pressure are facilitated by the adiabatic operation which allows the use of refractory lined vessels [4]. Texaco and Shell developed non-catalytic POM processes that offer high syngas yield [5,6], but operation is challenging by the high temperatures, required residence time and coke formation. CPOM uses a bifunctional combustion/steam reforming catalyst, using noble (Pt, Rh, Ir, Pd) and non-noble (Ni, Co) metals, and requires a very short residence time (1-40 ms). The O_2/CH_4-ratio of the feed allows adjusting the H_2/CO-ratio of the produced syngas. Feeding oxygen, syngas with a low H_2/CO-ratio (~2) can be produced, well suited for methanol synthesis, but very high maximum temperatures are reached (~1500°C) and coke formation, sintering and plastification and related catalyst deactivation are difficult to avoid [4,7]. A costly air separation unit is also required [8]. Air instead of oxygen can be used to lower the maximum temperature in the reactor and the rate of coke formation [4], but, except for ammonia synthesis, requires N_2 removal from the syngas. In autothermal reforming (ATR), steam is added to the feed, allowing negligible coke formation [8]. Hydrogen and / or CO_2 are also sometimes mixed with the feed but are less efficient in reducing coke formation [4]. The energy efficiency of SMR is 70-85%, whereas that of POM and ATR is 60-75% [9–11]. The latter is explained by the energy consumption of the required air separation unit (ASU). Cormos et al. [9] reported a hydrogen efficiency of 73.7% for SMR and of 67.7% for ATR. In this context, autothermal Chemical Looping Reforming (a-CLR) is studied as an alternative technology that facilitates capturing CO_2, eliminates the need for feeding pure oxygen and improves the overall energy efficiency [12,13]. The most widely studied a-CLR configuration consists of a dual-fluidized bed reactor system with a bubbling bed fuel reactor (FR) and a riser type air reactor (AR), as shown in Figure 1 [14]. In the AR the oxygen carrier (OC) particles are oxidized by air, while in the FR they are reduced by the methane and syngas and then act as catalyst for steam methane reforming. The OC used in a-CLR can be mono- or polymetallic metal oxides of, e.g., Ni, Fe, Cu, Ce, Co, and perovskite structure composites [15–20]. To adjust the H_2/CO ratio in the produced syngas for different successive processes and to recycle CO_2, co-feeding CO_2 is considered [21,22]. This, however, typically increases the risk of coke formation [23,24].

Various experimental studies focused on proof of concept. Chiron et al. [25] studied a-CLR in a micro-fixed bed reactor and concluded that the OC should maintain a low oxidation state to prevent oxidation of H_2. Ryden et al. [26,27], Pröll et al. [28], Diego et al. [29,30], Ortiz et al. [31] studied a-CLR in fluidized bed (FB) systems from small scale batch to 140 kW continuously operated dual-FB. With steam to carbon ratios of 0-0.7, a methane conversion of around 96% was achieved at temperature of 750 – 900 ^{o}C, which was very close to equilibrium conversion. In addition, no coke formation was observed. Autothermal operation was, however, difficult to achieve. Pröll et al. [28] used, e.g., a cooler in the AR to withdrawn heat to maintain the desired operation temperature independent of the global air to fuel ratio. Excess heat is, however, usually not desired in syngas production. Ortiz et al. [31] used a furnace to maintain the desired temperature, so that autothermal operation was hard to verify. Simulations can, on the other hand, be used to study the conditions allowing autothermal operation. A limited number of papers deal with the modeling and simulation of a-CLR. Ortiz et al. [32] investigated the heat balance and hydrogen yield in a-CLR with the assumption that all the reactions reach equilibrium. They concluded that the molar NiO-to-CH_4 feed ratio should be 1.2 to maintain autothermal operating, and that the maximum H_2 yield can be 2.75 mol H_2 per mol CH_4 after the water-gas-shift (WGS) reaction. More detailed simulations accounting for reaction kinetics were conducted by Diglio et al. [33] on a dual fluidized bed a-CLR system with a bubbling fluidized bed (BFB) fuel reactor (FR) and a riser air reactor (AR). The simulations, however, assumed that the gas and solids are well-stirred in the BFB, which may not be valid, especially for the gas phase. Wang et al. [34] used a two-fluid CFD model coupled with reaction kinetics to simulate CLR. The results matched well with experiments, but were limited to a lab scale reactor FR with low superficial gas velocity. The required reactor design and operating conditions to operate at commercial scale and realize autothermal operation have so far not been comprehensively studied. The energy efficiency of commercial scale a-CLR has also not been reported so far.

In this work, a 1-D coupled AR-FR model was developed that accounts for the essential features of the fluid dynamics of the BFB and riser, and the detailed reaction mechanism and kinetics. The model allows investigating the effect of the main operating parameters and OC properties on the reactor performance and evaluating scale-up of the technology. The detailed design of interconnections between the reactors is not addressed. The paper focuses on verifying if the reactor dimensions and solids circulation rate required for commercial operation are realistic. A carbon stripper is e.g. needed for the solids leaving the FR. The stripper is not shown in Figure 1 and was considered working perfectly in the simulations carried out.

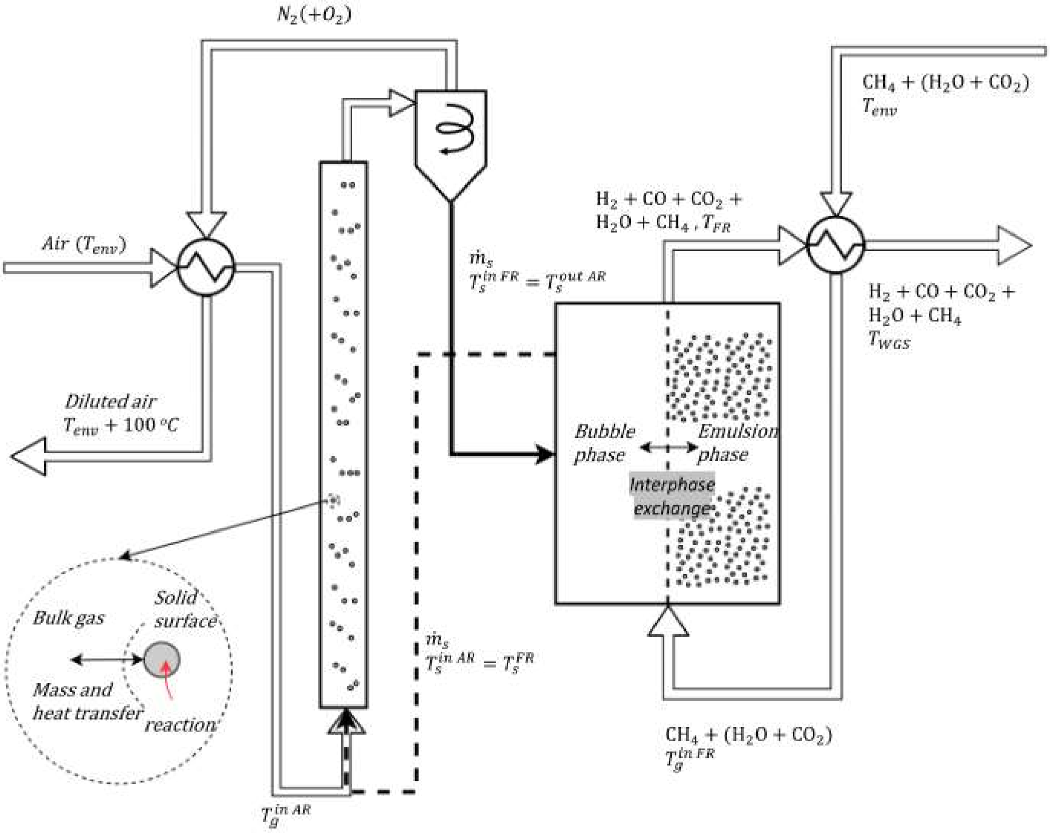

Figure 1. Schematic representation of the simulated a-CLR system.

The model was validated using data of a 140 kW dual fluidized bed CLR unit from Pröll et al. [28]. A commercial a-CLR unit with the capacity of 50 conventional SMR tubes is then studied. The dimensions of the FR were chosen to allow achieving a methane conversion above 95% with the reactor size as small as possible, which was done by simulating the FR with a variety of dimensions. The dimensions of the AR were chosen to allow achieving a high O_2 conversion with an acceptable solids circulation rate and moderate temperature rise in the AR, which was done by simulation the AR with a variety of feed gas velocities and solids circulation rates.

With the obtained design, the influence of the FR operating temperature, the fuel feed rate, the steam-to-methane feed ratio and the CO_2-to-(CO_2+H_2O) feed ratio on the process performance was studied, including risk of coke formation. A rough estimation of the energy efficiency of commercial scale a-CLR is also extracted from the simulations.

2 a-CLR model

The a-CLR unit considered in this work and the material flows are shown in Figure 1. Because of the short residence time required for slightly oxidizing the OC, a riser type AR is used. The reforming reactions in the FR are strongly endothermic and operation at high temperature and sufficiently high gas-catalyst (OC) contact times are required to achieve a sufficiently low methane slip. A BFB is used to ensure temperature uniformity and efficient heat transfer. The OC/catalyst considered in this work was $6.24\ [mol_{Ni}/kg_s]$ (on reduced basis), corresponding to 47% of free NiO on Al_2O_3. Its properties can be found in Table 1.

Table 1. Catalyst/oxygen carrier properties [35].

Support	Al_2O_3	
Ni concentration in reduced state	6.24	$[mol_{Ni}/kg_s]$
Oxygen carrier density	1515	$[kg_s/m_s^3]$
Equivalent diameter	250	$[\mu m]$

Note that 250 µm particles are used to allow a sufficiently high gas and gas-solids slip velocity, i.e., without causing entrainment. Diffusion limitations can, however, still be considered negligible. The durability of the catalyst is critical for fluidized bed operation. Long duration testing showed that the loss of fines decreased slowly with time, with the attrition becoming less predominate after the first 100 h [36]. A particle lifetime of 33,000 h was estimated from the data.

2.1 Reaction mechanism and kinetics

The intrinsic kinetics of the oxidation and reduction of Ni supported on Al_2O_3 and of the reactions catalyzed by Ni have been extensively studied in the literature. Interfacial gas-solid mass and heat transfer and intraparticle species transport have also been addressed [37].

In the FR, the NiO formed in the AR is reduced with H_2, CH_4 and CO, while reduced Ni catalyzes the steam reforming and WGS reactions. Focusing on transport limitations and the nucleation-and-growth nature of the NiO reduction, different models to describe the progress of the reaction have been proposed, e.g. empirical reaction order, Avramie-Erofe'ev (AEn), shrinking core and grain models, as summarized in [38,39]. Manukyan et al. [39] studied the NiO reduction, and found that an AEn model described well their experimental observations at low temperature, 543-773 K, implying both nucleation and diffusion controlled reaction. At 1173-1593K, however, the measured exponent of the AEn model increases with temperature and approaches 1, implying nucleation becomes less rate determining. A one-dimensional diffusion could accurately explain the observed reduction rate. Rodriguez et al. [40] studied the reduction of NiO with hydrogen using time resolved X-ray diffraction. They concluded surface oxygen defects play an important role in the dissociation of H_2 and adsorbed hydrogen can induce the migration of O vacancies. Richardson et al. [41] found that hydroxyl groups on the catalyst surface inhibit NiO reduction and observed that co-feeding steam had an important effect on the NiO reduction. Abad et al. [42] found, however, that H_2O and CO_2 have no effect on the reduction of NiO at 873-1273K. There is some consensus on essential steps in the reduction of NiO. For the solid NiO, the reduction involves formation of Ni nuclei, confirmed by in-situ XRD [39]. For the gas phase reducing species, adsorption and dissociation on the catalyst surface, reaction of surface species to break the Ni-O bond and desorption of product species have been identified [41]. The kinetics of the oxidation and reduction of Al_2O_3 supported Ni by O_2, H_2, CO and CH_4 was studied by Ipsakis et al. [43], Dueso et al. [44,45] and Dewaele and Froment [46]. Based on the experimental observations, it is assumed that, in the presence of NiO, CH_4, H_2 and CO are completely oxidized to the thermodynamically favored H_2O and CO_2 [47–49] and that these reactions can be considered irreversible. Based on a shrinking core model, reaction rate expressions that were derived for NiO reduction reactions R2, R3 and R4 by Abad et al. [50] are adopted in this work:

$$r_{Ri} = -3(C_{Ni}^{tot})^{\frac{1}{3}}(C_{NiO})^{\frac{2}{3}}k_{Ri}\left(C_g^{Ri}\right)^{n_{Ri}}, i = 2,3,4;\ C_g^{Ri} = C_{H_2}, C_{CH_4}, C_{CO}. \quad (1)$$

For the steam methane reforming reactions, it is widely accepted that CH_4 adsorbs on the active sites l associated with reduced Ni, and is dehydrogenated to CH_3-l, CH_2-l, CH-l and C-l by the interaction with other active sites l. Oxygen adsorbed on active sites l or lattice oxygen, react with the carbon containing surface species to form CH_3O-l, CH_2O-l, CHO-l, CO-l and CO_2-l [46,51,52]. On a OC surface with high NiO coverage, CH_3O-l surface species are favored because active sites l are less abundant [52]. Considering that in practice the OC can be only slightly oxidized in the AR, it can be assumed that in the FR, NiO reduction and CH_4 reforming take place in parallel. For the steam methane reforming reactions, Hou and Hughes [53] considered that reactions R5 and R7 occur via the same elementary steps, while Xu and Froment [51] recognized that R5 and R7 proceed via different elementary steps and different reaction intermediates. This independent route to CO_2 and CO has been confirmed by both

DFT [54] simulation and experimental studies [55]. Langmuir-Hinshelwood Hougen-Watson type rate expression for the steam reforming and WGS reactions (R5-R7) on a fully reduced Ni-catalyst were derived based on experimentally identified rate determining steps:

$$r_{R5} = \frac{k_{R5}}{p_{H_2}^{2.5}}(p_{CH_4}p_{H_2O} - \frac{p_{H_2}^3 p_{CO}}{K_{R5}})/(\mathrm{DEN})^2 \tag{2}$$

$$r_{R6} = \frac{k_{R6}}{p_{H_2}}(p_{CO}p_{H_2O} - \frac{p_{H_2} p_{CO_2}}{K_{R6}})/(\mathrm{DEN})^2 \tag{3}$$

$$r_{R7} = \frac{k_{R7}}{p_{H_2}^{3.5}}(p_{CH_4}p_{H_2O}^2 - \frac{p_{H_2}^4 p_{CO_2}}{K_{R7}})/(\mathrm{DEN})^2 \tag{4}$$

with:

$$\mathrm{DEN} = 1 + K_{CO}p_{CO} + K_{H_2}p_{H_2} + K_{CH_4}p_{CH_4} + K_{H_2O}p_{H_2O}/p_{H_2} \tag{5}$$

The presence of NiO affects the catalytic activity for steam methane reforming and WGS as steam cannot adsorb and form adsorbed O-l species on NiO. Froment et al. [4,46,56] concluded that catalyst is deactivated for the SMR and WGS reactions even when it is partially oxidized and the catalyst would be completely deactivated with 20% oxidation. The influence of the presence of NiO on the SMR and WGS reaction kinetics was studied by De Groote and Froment [4], proposing the following deactivation function which was adopted in this work:

$$\varphi_{NiO} = (C_{Ni}/(C_{Ni} + C_{NiO}))^{12} \tag{6}$$

with

$$r_j = \varphi_{NiO} r_j^{Ni}, j = R5, R6, R7 \tag{7}$$

Coke formation also leads to catalyst deactivation and has to be avoided. Two coke formation and gasification reactions were considered, R8 and R9 accounting for methane cracking and the Boudouard reaction. Based on a detailed reaction mechanism, included in Figure 2, Snoeck et al. [52,53]derived an expression for the initial net rate of coke formation by methane cracking, reaction (8) [56], and by the Boudouard reaction, reaction (9) [57], that is, on an un-coked catalyst. These expressions can be used for an a posteriori evaluation of the risk of coke formation and can be written as:

$$r_{Crk} = k_{Crk}K_{CH_4}\left(p_{CH_4} - p_{H_2}^{2}/K_{Crk}\right)/\left(1 + p_{H_2}^{1.5}/K_r'' + K_{CH_4}p_{CH_4}\right)^2 \qquad (8)$$

$$r_B = k_B K_{CO}\left(p_{CO} - p_{CO_2}/K_B p_{CO}\right)/\left(1 + K_{CO}p_{CO} + p_{CO_2}/\left(K_{O,CO_2}k_{CO}p_{CO}\right)\right)^2 \qquad (9)$$

Hatcher et al. [35] studied the oxidation of Ni supported on calcium aluminate by O_2 in a micro-electro-balance reactor at temperature of 276 to 611 °C and assuming that intraparticle species concentration gradient could be neglected. They showed that O_2 first adsorbs and dissociates on the Ni sites followed by a rate determining reaction with Ni, leading to Hougen-Watson rate expression:

$$r_{R1} = 2\frac{k_{R1}K_{O_2}p_{O_2}^{s}C_{Ni}^{2}}{1 + K_{O_2}p_{O_2}^{s}} \qquad (10)$$

In recent literature [42,43,45,58], much faster oxidation kinetics is reported, indicating transport limitations were probably encountered by Hatcher et al. [35]. Whereas the functional form of (10) was adopted in this work, the pre-exponential factor was re-estimated based on the recent literature data.

The reaction mechanism considered in this work is shown in Figure 2 and accounts for reduction by H_2, CH_4 and CO, the different reforming reactions and the WGS. The possible reaction of coke with NiO is not included in the analysis and requires further investigations. Experimental observations by Galvita et al. [19] on a Ni/CeO_2-Fe_2O_3 catalyst show that surface carbon can indeed be oxidized by lattice oxygen from the metal oxides. The global reactions in the a-CLR system that are typically considered are summarized in Table 2. The required thermodynamic and rate constants to calculate the reaction rates can be found in Table A. 1.

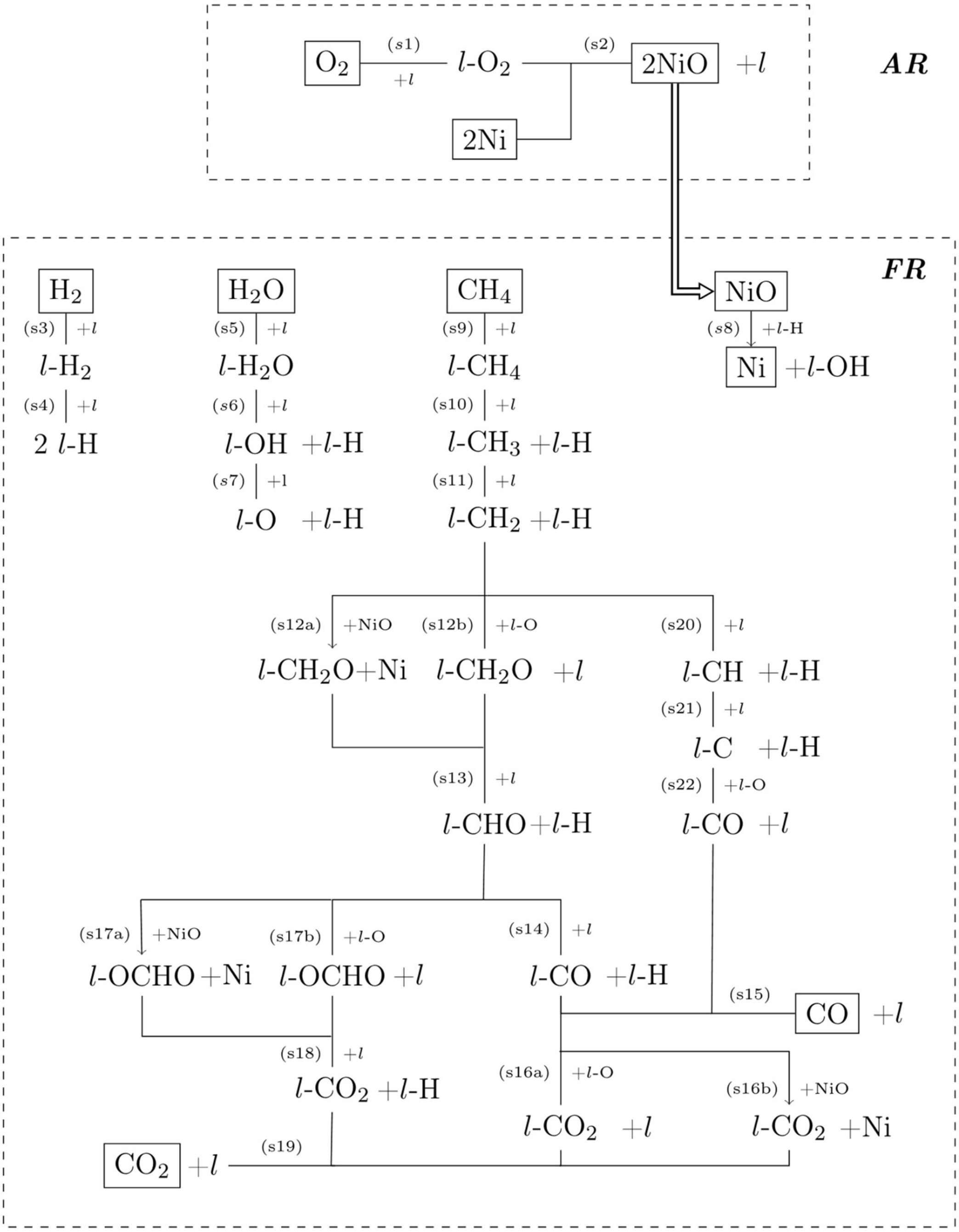

Figure 2. Reaction mechanism for the OC oxidation (AR) and reduction (FR), the steam methane reforming and the coke formation and gasification.

Whereas the rate expressions for the oxidation of Ni, the steam methane reforming reactions, the water-gas-shift reaction, and the coke formation and gasification reactions (methane cracking, Boudouard reaction) reflect the detailed reaction mechanism shown in Figure 2, this is not the case for the NiO reduction reactions for which no rate expressions based on a detailed reaction mechanism could be found in the literature.

Table 2. Global reactions in a-CLR.

Global reactions	Elementary steps involved
$R1: 2\mathrm{Ni} + \mathrm{O_2} \rightarrow 2\mathrm{NiO}$ $-\Delta H = 469.2\ \mathrm{kJ/mol}$	(s1), (s2)
$R2: \mathrm{NiO} + \mathrm{H_2} \rightarrow \mathrm{Ni} + \mathrm{H_2O}$ $-\Delta H = 13.9\ \mathrm{kJ/mol}$	(s3), (s4), (s8), (s6), (s5)
$R3: 4\mathrm{NiO} + \mathrm{CH_4} \rightarrow 4\mathrm{Ni} + 2\mathrm{H_2O} + \mathrm{CO_2}$ $-\Delta H = -137.4\ \mathrm{kJ/mol}$	(s5), (s6), (s8), (s9), (s10), (s11) (s12a), (s13) with (s14), (s16b), (s19) or (s17a), (s18), (s19)
$R4: \mathrm{NiO} + \mathrm{CO} \rightarrow \mathrm{Ni} + \mathrm{CO_2}$ $-\Delta H = 47.6\ \mathrm{kJ/mol}$	(s15), (s16b), (s19)
$R5: \mathrm{CH_4} + \mathrm{H_2O} \overset{\mathrm{Ni}}{\leftrightarrow} \mathrm{CO} + 3\mathrm{H_2}$ $-\Delta H = -226.7\ \mathrm{kJ/mol}$	(s3), (s4), (s5), (s6), (s7), (s9), (s10),(s11), (s12b), (s13), (s14), (s15). (s14 as r.d.s)
$R6: \mathrm{CO} + \mathrm{H_2O} \overset{\mathrm{Ni}}{\leftrightarrow} \mathrm{CO_2} + \mathrm{H_2}$ $-\Delta H = 33.7\ \mathrm{kJ/mol}$	(s3), (s4), (s5), (s6), (s7), (s15), (s16a), (s19). (s16a as r.d.s.)
$R7: \mathrm{CH_4} + 2\mathrm{H_2O} \overset{\mathrm{Ni}}{\leftrightarrow} \mathrm{CO_2} + 4\mathrm{H_2}$ $-\Delta H = -193.0\ \mathrm{kJ/mol}$	(s3), (s4), (s5), (s6), (s7), (s9), (s10), (s11), (s12b), (s13), (s17b), (s18), (s19). (s17b as r.d.s)
$R8: \mathrm{CH_4} \overset{\mathrm{Ni}}{\leftrightarrow} \mathrm{C} + 2\mathrm{H_2}$ $-\Delta H = -74.8\ \mathrm{kJ/mol}$	(s3), (s4), (s9), (s10), (s11), (s20), (s21)
$R9: 2\mathrm{CO} \overset{\mathrm{Ni}}{\leftrightarrow} \mathrm{CO_2} + \mathrm{C}$ $-\Delta H = 172.5\ \mathrm{kJ/mol}$	(s15), (s16a), (s19), (s22)

2.2 Fluid dynamics and reactor model

Steady state reactor simulations are aimed at. Both the AR and FR are considered operated adiabatically. Under typical commercial conditions, the riser AR operates at sufficiently high Reynolds number to allow using a 1D model based plug flow and slip between the phases [37]. A heterogeneous model is adopted that accounts for interfacial mass and heat transfer limitations [59]. The species continuity equations for the gas and solid surface species are:

$$\frac{d\hat{F}_{O_2}}{dz} = -k_g a_v \left(p_{O_2} - p_{O_2}^s\right) \tag{11}$$

$$\frac{\dot{m}_s}{\Omega} \frac{dC_{O_2}^s}{dz} = k_g a_v \left(p_{O_2} - p_{O_2}^s\right) - r_{R1} \rho_s \left(1 - \varepsilon_g\right) \tag{12}$$

$$\frac{\dot{m}_s}{\Omega} \frac{dC_{Ni}}{dz} = -2 r_{R1} \rho_s \left(1 - \varepsilon_g\right) \tag{13}$$

The energy conservation equation for the gas and solids are:

$$u_{sg} \rho_g \overline{C_{p,g}} \frac{dT}{dz} = -h_f a_v (T - T_s) \tag{14}$$

$$\frac{\dot{m}_s C_{p,s}}{\Omega} \frac{dT_s}{dz} = h_f a_v \, (T - T_s) + r_{R1} (-\Delta H_{R1}^r) \rho_s \left(1 - \varepsilon_g\right) \tag{15}$$

The pressure drop is calculated following Breault and Mathur [60], accounting for the hydrostatic pressure drop, gas-wall friction and solid-wall friction:

$$-\frac{dp_{tot}}{dz} = \rho_s g \left(1 - \varepsilon_g\right) + \rho_g g \varepsilon_g + \frac{2 \eta_s \rho_s u_{ss}^2}{\left(1 - \varepsilon_g\right) d_t} + \frac{2 \eta_g \rho_g u_{sg}^2}{\varepsilon_g d_t} \tag{16}$$

For the BFB FR, the two-phase model developed by Kunii and Levenspiel [61] is adopted. It considers a particle-free bubble phase and an emulsion phase with the particles and the minimum amount of gas to reach the minimal fluidization velocity in the reactor. Plug flow is assumed for the bubble phase. Because of the back-mixing in the emulsion phase, effective axial dispersion is accounted for in the emulsion gas species continuity equations. The gas species continuity equations for the bubble and emulsion phase can then be written as:

$$\frac{d\left(\hat{F}_{Ab}\right)}{dz} = -k_I(C_{Ab} - C_{Ae}) + \ \Delta F_{A,Ei} \tag{17}$$

$$\frac{d\left(\hat{F}_{Ae}\right)}{dz} = \frac{d}{dz}\left(\frac{D_{eg}}{f_{eg}u_{eg}}\frac{d\hat{F}_{Ae}}{dz}\right) + k_I(C_{Ab} - C_{Ae}) + R_A\rho_s f_{es} - \ \Delta F_{A,Ei} \tag{18}$$

The solids composition is often assumed uniform in a BFB. With fast reactions and continuous solids feeding and removal, a well-mixed particle bed can, however, not be guaranteed. Axial mixing of the solids is therefore also accounted for through an axial dispersion type term:

$$u_{sp}\frac{dC_{NiO}}{dz} = D_{es}\frac{d^2C_{NiO}}{dz^2} + R_{NiO} \tag{19}$$

In contrast to a CSTR type model for the solids, Eq. (19) allows accounting for full reduction of the catalyst in the FR. The pressure drop in the BFB is dominated by the hydrostatic contribution, so that:

$$-\frac{dp}{dz} = \bar{\rho}g \approx \rho_s f_{es} g \tag{20}$$

The FR is assumed isothermal because of the relative low temperature difference between the AR and the FR, the efficient solids mixing in the FR and the high thermal conductivity and heat capacity of the solids. The temperature can then be calculated from an overall heat balance:

$$\dot{m}_s^{FR\ in}h_s\left(T_s^{FR\ in}\right) + \sum_A \dot{m}_A^{FR\ in}h_A\left(T_g^{FR\ in}\right) = \dot{m}_s^{FR\ out}h_s(T_{FR}) + \sum_A \dot{m}_A^{FR\ out}h_A(T_{FR}) \tag{21}$$

Mass and heat transfer limitations between the gas and solids in the emulsion phase are considered negligible [37]. The reaction rates are, hence, calculated using C_{Ae}. The absence of gas-solid mass transfer limitations in the emulsion phase was confirmed a posteriori from the simulation results applying the Mears [62] criterion: $\Delta C_{A,fs} = r_A \rho_s d_p / 6k_g < RI_{im,r} C_{Ae}/n$, with $RI_{im,r}$ the maximum error on the reaction rate if gas-solid mass transfer limitations are neglected. Using the Davidson and Harrison [63] correlation for the mass transfer coefficient, $k_g = (1-\varepsilon)^{0.5}\varepsilon^{-1}u_{sg}\left(Re_p\right)^{-0.6}Sc^{-2/3}$, assuming a quasi-first-order SMR reaction and focusing on the reactor inlet where the reaction rate is highest, about 0.03 $[mol_{CH_4}/kg_{cat} \cdot s]$ in the commercial scale reference case, discussed later, $k_g = (1-0.63)^{0.5} \cdot 0.63^{-1} \cdot 0.05 \cdot (2.5 \cdot 10^{-4} \cdot 0.05 \cdot 0.4/3.3 \cdot 10^{-5})^{-0.6} = 0.27 \left[m_g^3/(m_i^2 \cdot s)\right]$ and a maximum error on the reaction rate of less than 1% is confirmed: $\Delta C_{A,fs} < 0.03 \cdot 1515 \cdot 250 \cdot 10^{-6}/6 \cdot 0.27 = 0.007 < 1\% \cdot 1 = 0.01 \left[mol_{CH_4}/m_g^3\right]$.

In fluidized beds of Geldart B particles, the presence of a cloud is important for the bubble-emulsion phase mass transfer [59]. Sit and Grace [64] also noted that in freely bubbling beds, bubble-emulsion phase mass transfer can be significantly enhanced by bubble interactions so that Davidson's correlation [63], that was derived from experiments with isolated bubbles, underestimates the bubble-emulsion phase mass transfer coefficient. Detailed simulations [65] [65]and IR transmission technique experiments [66] were recently used to study bubble-emulsion phase mass transfer with Geldart B particles and derive correlations for the bubble-emulsion phase mass transfer coefficient in bubbling fluidized beds. Both groups observed that the diffusive contribution to the mass transfer was negligible, the convective contribution being dominant, and that the bubble-emulsion phase mass transfer was considerably more efficient than predicted by Davidson's model. The correlation of Medrano et al. [66] was adopted in this work, as its derivation did not depend on a literature correlation for the bubble rise velocity:

$$k_I = \frac{4}{d_b}\frac{2.6u_{sg}}{\pi} \tag{22}$$

The void fraction in the emulsion phase is assumed to equal the void fraction at minimum fluidization condition, ε_{mf}. To account for the expansion due to reactions R3, R5 and R7 involving methane and to limit the void fraction in the emulsion phase to ε_{mf}, an excess gas transfer term from the emulsion phase to the bubble phase, $\Delta F_{A,Ei}$, has to be introduced in Eqs. (17) and (18) and is calculated according to Yan et al. [72].

For the initial bubble diameter, the model of Miwa [67] is recommended when using an orifice distributor with high gas velocities [59]:

$$d_{b0} = 0.376\left(u_{sg} - u_{mf}\right)^2 \tag{23}$$

For the bubble growth, the correlation of Mori and Wen [68] which limits the maximum bubble size is recommended with Geldart B particles [59]:

$$\frac{d_{bm} - d_b}{d_{bm} - d_{b0}} = \exp\left(-\frac{0.3z}{d_t}\right) \tag{24}$$

with:

$$d_{bm} = 1.638\left[0.25\pi d_t^2\left(u_{sg} - u_{mf}\right)\right]^{0.4} \tag{25}$$

The Mori and Wen [68] correlation was reported to be applicable for $0.3\ m \leq d_t \leq 1.3\ m$, $60\ \mu m \leq d_p \leq 450\ \mu m$, $0.005 \leq u_{mf} \leq 0.2\ m/s$ and $u_{sg} - u_{mf} \leq 0.48\ m/s$, but a comparison with data in smaller diameter beds, down to 7.6 cm, was also made. For $d_t \leq 0.3\ m$, still a relatively good fit with the data was found, but the uncertainty on the bubble diameter prediction increased. The correlation assumes a freely bubbling bed which requires

$d_b \leq 0.3d_t$. Mori and Wen [68] suggested that use of their correlation with beds with $d_t \geq 1.3\ m$ is possible, but requires evaluating and eventually modifying the correlation for d_{bm} which is based on the assumption of the formation of a single bubble track. Horio and Nonaka [69] postulated, however, that the formation of a maximum bubble diameter is the result of an equilibrium of successive coalescence and splitting of bubbles and derived a generalized correlation that was found to predict realistic maximum bubble sizes and to converge with the Mori and Wen [68] equation for the case of Geldart B particles. The Mori and Wen [68] correlation for d_{bm} is therefore also used for the commercial scale FR simulations, as recommended in Kunii and Levenspiel [59].

For the bubble rise velocity, Davidson and Harrison [63] and Kunii and Levenspiel [61] noticed that various reported correlations for the bubble rise velocity result in a problematic prediction when used with Geldart B particles and operation at relatively high gas velocities. The gas flow rate through the emulsion phase is the gas flow rate required for minimum fluidization of the bed, so that the superficial bubble phase velocity can be calculated from $f_b u_b = u_{sg} - u_{mf}$. It is seen that in order to prevent the bubble volume fraction in the bed, f_b, to become larger than 1, the value of the bubble rise velocity, u_b, has to be at least equal to $u_{sg} - u_{mf}$. This is not the case with many of the correlations reported in the literature, as also observed in the FR simulations where the high gas velocities further increase as a result of the reactions. Davidson and Harrison [63] therefore proposed to calculate the bubble rise velocity as:

$$u_b = u_{sg} - u_{mf} + u_{br} \tag{26}$$

with u_{br} calculated as the single bubble rise velocity:

$$u_{br} = 0.71(gd_b)^{0.5} \tag{27}$$

Based on non-invasive and non-intrusive electrical capacitance tomography measurements in fluidized beds of Geldart B particles, Li et al. [70] proposed a correlation for the bubble rise velocity that is similar to that of Davidson and Harrison [63], but using the correlation of Werther [71] for the calculation of u_{br}:

$$u_{br} = \Psi(gd_b)^{0.5} \tag{28}$$

with:

$\Psi = 0.64, \text{for } \mathrm{d_t} < 0.1\ m, \Psi = 1.6\mathrm{d_t^{0.4}} \text{ for } 0.1 < d_t < 1\ m$, and $\Psi = 1.6 \text{ for } \mathrm{d_t} > 1\ m$.

The correlation of Li et al. [70] was adopted for both the pilot plant and commercial scale FR simulations.

The axial dispersion of the solids in the bed is typically more pronounced in larger-diameter reactors. Kunii and Levenspiel [59] showed that the axial dispersion in rather small-diameter beds is directly related to the gas velocity and well described by:

$$D_{es} = 0.06 + 0.1u_{sg} \tag{29}$$

The values predicted by the correlation fit well with data from a 15 cm-diameter bed [59] and this correlation was used for the simulation of the pilot plant FR with a diameter of 15.9 cm. For large-diameter beds, Kunii and Levenspiel [59] proposed:

$$D_{es} = 0.3d_t^{0.65} \tag{30}$$

, which was found to account well for the experimentally observed more rapid axial mixing of solids with increasing reactor diameter. This correlation was used for the simulation of the commercial scale a-CLR unit. The constitutive equations and boundary conditions are summarized in Table A. 2 and Table A. 3. Gas phase density variations are calculated through the ideal gas law. The required thermodynamic data are taken from the website of National Institute of Standards and Technology (https://webbook.nist.gov/chemistry/).

2.3 Solution algorithm

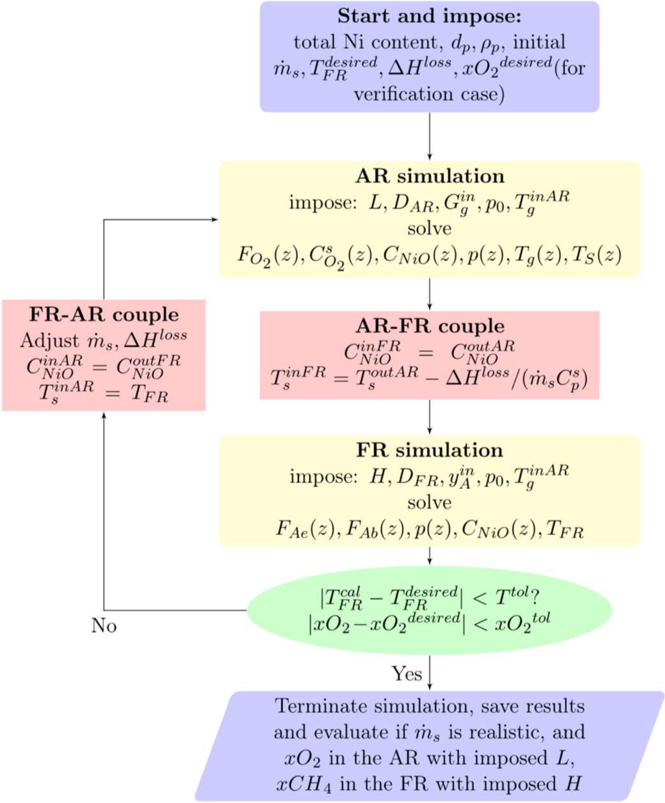

Figure 3. Numerical solution algorithm

Figure 3 summarizes the solution algorithm. Simulations are carried out with given reactor dimensions. The two reactors are coupled via the inlet conditions. The desired FR temperature is imposed accounting for equilibrium limitations of the steam methane reforming reactions while the actual FR temperature is calculated according to Eq. (21). The desired O_2 conversion is only imposed in the validation case. In that case, a heat loss of about 10–15 kW needs to be accounted for. Furthermore, a cooler in the AR extracts heat to ensure the desired FR temperature is reached, independent of the global air to CH_4 ratio. The heat loss and cooling power, in total noted as ΔH^{loss} in the simulation, were accounted by reducing the solids feed temperature to the FR. The ΔH^{loss} was adjusted to ensure that the difference between the calculated and the desired FR temperature was less than 0.1 K, whereas the solids circulation rate was adjusted to ensure the calculated and imposed O_2 conversion differ less than 3%. To improve convergence, two PID algorithms were used. Typically, it is more difficult for the FR temperature to converged. In commercial scale case studies, the solids circulation rate, $\dot{m}_s$, is varied until the desired FR operation temperature is reached, with the heat loss, ΔH^{loss}, being assumed zero, so that autothermal operation is ensured. It was verified that the simulation results respect the C-, H- and O-balances and the stoichiometry of the reactions.

3 Results and discussions

3.1 Validation

The model is first validated by simulating the 140 kW dual fluidized bed a-CLR system as described in [28]. The FR diameter is 0.159 m, with a height of 3 m. The AR diameter is 0.15 m with a height of 4 m. The two reactors are interconnected by two loop seals. The detailed reactor dimensions are given in [73]. The air and fuel were fed at room temperature. Part of the steam used in the lower loop seal was mixed with the feed CH_4 to the FR, with an estimated steam-to-CH_4 feed ratio of 1/6. In what follows the methane, oxygen and Ni conversion will be discussed. The methane conversion is defined by:

$$x_{CH_4}(z) = \left(\hat{F}_{CH_4}^{in\,FR} - \hat{F}_{CH_4}(z)\right)/F_{CH_4}^{in\,FR} \qquad (31)$$

where $\hat{F}_{CH_4}(z)$ is the sum of methane flow rate in the bubble and emulsion phases. The oxygen conversion and Ni conversion are defined as:

$$x_{O_2}(z) = \left(\hat{F}_{O_2}^{in\,AR} - \hat{F}_{O_2}(z)\right)/\hat{F}_{O_2}^{in\,AR} \tag{32}$$

$$x_{Ni}(z) = \left(C_{Ni}^{in\,AR} - C_{Ni}(z)\right)/C_{Ni}^{in\,AR} \tag{33}$$

Experiments at three global air-to-CH_4 feed ratios and three different FR temperature [28] were simulated. The measured and simulated FR outlet composition is are shown in Figure 4. The trends are generally well predicted although the model predicts somewhat lower outlet H_2O fractions and higher outlet H_2 and CO fractions. This is attributed to the experimentally observed slightly higher oxygen flow rate from the AR to the FR, as seen from the oxygen conversion in Figure 5 discussed hereafter.

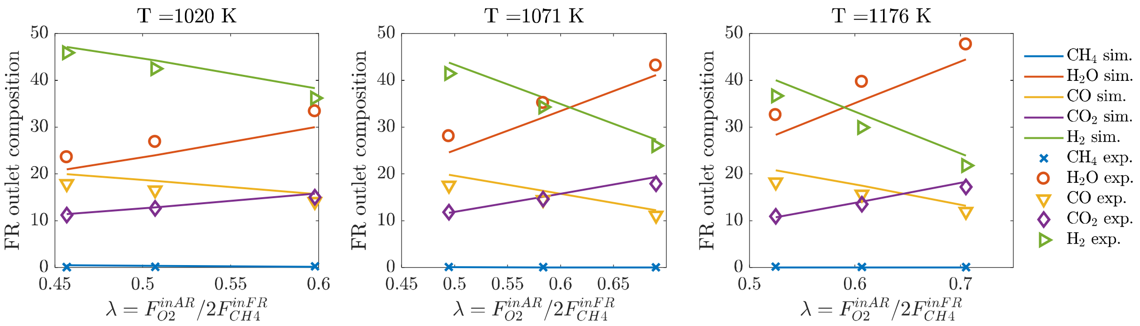

Figure 4. FR outlet composition as a function of global excess air to fuel feed ratio at T_{FR}=1020K, T_{FR}=1071K and T_{FR}=1176K. Lines: simulation results. Markers: experiments data in Pröll et al. [28]. Refer to [28,73] for detailed reactors dimensions and operation conditions.

Figure 5 shows the required solids circulation rate to reach the desired FR operating temperature, T_{FR}, as well as the resulting O_2 conversion as a function of the global excess air to fuel feed ratio and for different T_{FR}. The O_2 conversion and solids circulation rate are well predicted, except at the higher FR operating temperatures when the air-to-CH_4 feed ratio is high (Figure 5). Under such conditions, the O_2 conversion is somewhat under predicted, whereas the solids circulation rate is significantly over predicted, by up to 75%. This can be explained by a different reactivity of the oxygen carrier (OC), in particular at high temperature, or by the falsification of the intrinsic reaction kinetics in the measurements reported in the literature. Interfacial mass transfer limitations may have been encountered, especially when the reaction rate is high, i.e. at high temperature [37]. The OC oxidation kinetics at high temperature would then be under predicted in the simulations, leading to an under prediction of the O_2 conversion and an over prediction of the solids circulating rate. The literature indeed reports some variation in the OC reduction and oxidation reactivity. Dueso et al. [45] reported a Ni-based OC with very fast reduction and oxidation rates, requiring around 15s to complete oxidation with O_2 or reduction with CH_4/CO/H_2 or O_2 at temperature ranges from 973 to 1223 K. Zhou et al. [38], on the other hand, reported that the time needed complete oxidation of their Ni-based OC was about 2 min at 1073K. With the OC oxidation kinetics used in the work, 80 s is needed for 80% oxidation with air at 1073K starting from a completely reduced OC, which is a relatively average value compared to values reported in the literature.

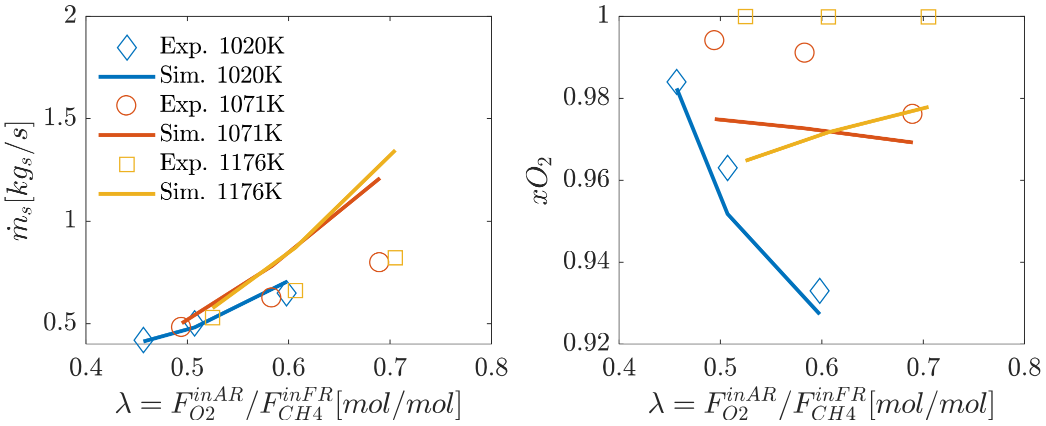

Figure 5. Required solids circulation rate to reach the desired FR operating temperature (T_{FR}=1020K, T_{FR}=1071K, T_{FR}=1176K) and the resulting O_2 conversion as a function of the global air to CH_4 feed ratio. Lines: simulation results. Markers: experimental data in Pröll et al. [28].

As an example, the axial concentration and reaction rate profiles in the FR operating at $T_{FR} = 1071\ \mathrm{K}$ and $\lambda = 0.45$ are shown in Figure 6, with both the mean and emulsion gas concentration profiles. The methane conversion increases fast in the first 0.2 m of the bed despite the oxidized catalyst being fed from the bottom. It is seen that most of the catalyst is reduced in the bottom of the FR and by CO and H_2. The catalyst is only slightly oxidized in the AR so that it remains sufficiently active for the SMR and WGS reactions. The evolution of the catalyst deactivation function is shown in Figure 6c. Figure 6b shows the gaseous species and NiO concentrations in the emulsion phase, which are closely related to the reaction rates. The methane concentration in the emulsion gas is seen to be significantly lower than the mean methane concentration, or that in the bubble phase. After about 0.3 meter in the bed, the methane concentration in the emulsion gas becomes very low, while the mean methane concentration continues to decrease slowly. Bubble-emulsion phase mass transfer clearly determines the performance of the reactor. Figure 6c shows the reaction rate profiles in the FR. The first steam methane reforming reaction is dominant in the first half meter of the reactor, but its rate rapidly decreases with decreasing methane concentration in the emulsion phase, reinforced by the isothermal operation of the FR in contrast with a conventional fixed bed steam reformer. NiO reduction continues throughout the reactor, confirming the finding of Pröll et al. [28] that NiO was not completely reduced in the FR. Because the steam-to-methane ratio in the feed gas is very low, the risk of coke formation is to be evaluated. As shown in Figure 6d, methane cracking and the Boudouard reaction have relatively low rates, but can lead to coke formation in the first 0.2 m of the FR. Higher up, the Boudouard reaction proceeds in the reverse direction and much faster than methane cracking, so that no net coke formation is to be feared. A high CO_2 concentration in the emulsion phase shifts the Boudouard reaction in the reverse direction, while a high H_2 concentration inhibits methane cracking and a high H_2O concentration pushes the WGS reaction which produces more CO_2 and H_2. The steam-to-methane ratio in the emulsion phase is also much higher than that in the feed gas shortly after the inlet, explaining a reduced risk of coke formation. Indeed, coke formation was not observed in [28].

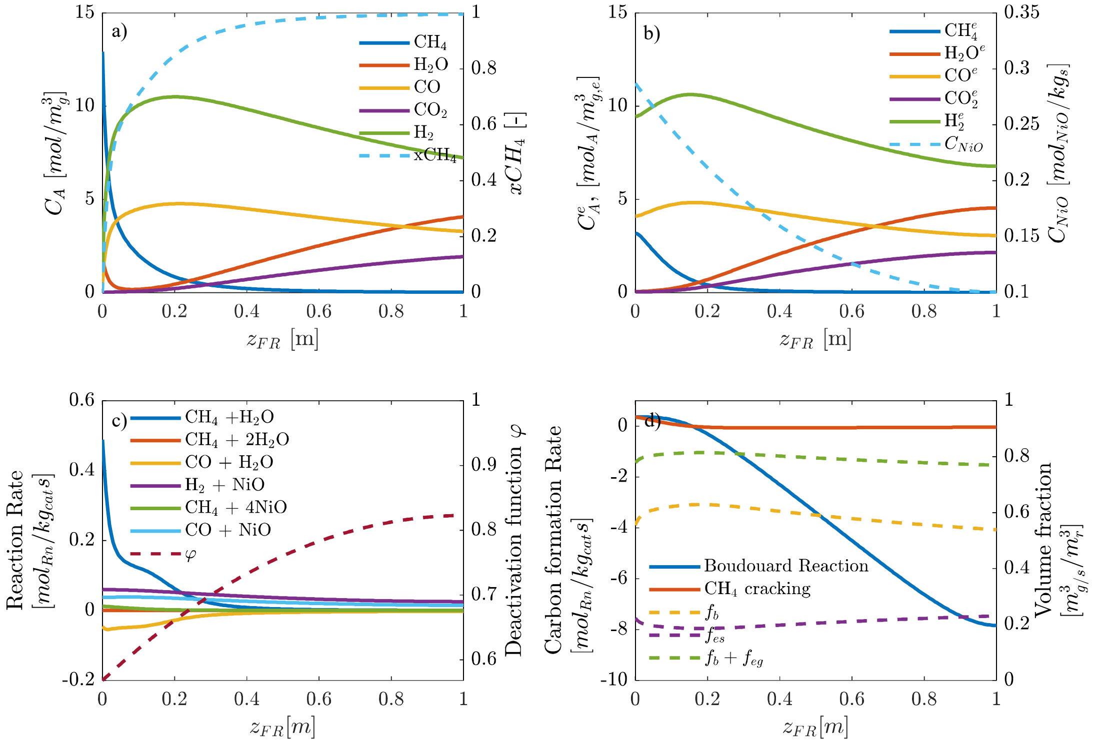

Figure 6. Axial profiles in the FR of the (a) mean species concentrations and methane conversion, (b) species concentrations in the emulsion phase, (c) reaction rates and (d) risk of coke formation and bubble, gas and solids volume fractions. Simulation of the pilot plant test of Pröll et al. [28] with $T_{FR} = 1071\ K$ and $\lambda = 0.45$.

3.2 Simulation of a commercial scale a-CLR unit

In a commercial a-CLR unit, the air fed to the AR and the fuel (mixture of methane, steam and/or CO_2) fed to the FR are pre-heated using respectively the gases exiting the AR and FR using two counter-current heat exchangers. The flue gas exit temperature from the AR pre-heater is considered 100 K above room temperature to guarantee sufficient driving force for heat transfer. The syngas exit temperature from the FR pre-heater is assumed 573K, as needed for the downstream WGS reaction. The feed temperatures of the air into the AR and the fuel mixture into the FR are calculated according to heat balances over the heat exchangers:

$$\dot{m}_{air}^{AR\ in} \int_{T_{env}}^{T_g^{AR\ in}} C_p^g dT + \dot{m}_g^{out} \int_{T_g^{AR\ out}}^{T_{env}+100} C_p^g dT = 0 \tag{34}$$

$$\sum_A \left(\dot{m}_A^{FR\ out} \int_{T_{FR}}^{T_{WGS}} C_{p,A} dT \right) + \sum_A \left(\dot{m}_A^{FR\ in} \int_{T_{env}}^{T_g^{,FR\ in}} C_{p,A} dT \right) = 0 \tag{35}$$

It was assumed that, in order to be competitive, an a-CLR unit should have the capacity of minimum 50 conventional reformer tubes, leading to a methane feed flow rate of 71.4 $[mol_{\mathrm{CH_4}}/s]$ [4]. The diameter of the FR is determined by the feed flow rate and the maximum allowable superficial gas velocity. Considering the volume expansion as a result of steam methane reforming reactions, the superficial gas velocity at the inlet of the FR should not be much higher than the minimum fluidization velocity, so that the gas velocity at the outlet of the FR can be kept sufficiently below the terminal velocity of the particles. After simulating the FR with different feed gas velocities, a 4 m diameter, 2 m long FR was selected to be appropriate for the 50-tube equivalent throughput aimed at. In previous chemical looping reforming studies [27,28,30] the methane conversion reached about 98% while the steam to methane ratio ranges from 0-0.5. In this work, the reference H_2O/CH_4 feed ratio was 0.23, and varied between 0.1 and 0.5 when investigating the effect of H_2O/CH_4 feed ratio. When CO_2 is co-fed, the $(H_2O+CO_2)/CH_4$ feed ratio was kept constant at 0.23.

In the AR riser, the air velocity should be higher than the transport velocity, u_{tr}, that is calculated according to [74]:

$$Re_{tr} = u_{tr} d_p \rho_g / \mu = 1.53 Ar^{0.5} \tag{36}$$

$$Ar = \rho_g \left(\rho_s - \rho_g \right) d_p^3 g / \mu^2 \tag{37}$$

At the feed temperature of 873K, $u_{tr} = 3.82\ [m_g^3/m_r^2 s]$. A too high superficial air velocity is to be avoided as it leads to an unrealistic riser height requirement. Ortiz et al. [32] determined an oxygen-to-methane feed ratio of 1.18 is required to allow autothermal operation when the gas/air inlet temperature is 750 K. In this work, if not specified, the air feed rate was fixed to have an oxygen-to-methane feed ratio of 1.35. The cross-sectional area is then determined by:

$$u_g^{in\ AR}\Omega_{AR}\rho_g^{T=873K} = G_{\mathrm{g}}^{in\ AR} = 1.35 \times 71.4 \times \left(M_{O_2} + M_{N_2} \times 0.79/0.21\right) \times 0.5 \qquad (38)$$

where $u_g^{in\ AR} > u_{tr}$. After simulating AR of different height with different gas feed velocities, a 10 m tall riser was chosen for an acceptable Ni conversion and adiabatic temperature rise in the AR. Finally, it was considered that both in the AR and the FR, gas and solids enter from the bottom and exit from the top. The reactor dimensions and feed flow rates of the reference commercial scale a-CLR unit simulation are summarized in Table 3. Note that with the retained reactor dimensions, with a 2 m tall FR and a 10 m tall AR, sufficient height should be available to install cyclones, loop seal, etc.

Table 3. Reactor dimensions and standard case operating conditions.

Parameters	d_{FR} [m]	H_{FR} $[m]$	T_{FR} [K]	$F_{\mathrm{CH_4}}^{\mathrm{in,FR}}$ $[mol/s]$
Value	4	2	1073	71.4
Parameters	$F_{\mathrm{H_2O}}^{in,FR}$ $[mol/s]$	$F_{\mathrm{CO}}^{in,FR}$ $[mol/s]$	$F_{\mathrm{CO_2}}^{in,FR}$ $[mol/s]$	$F_{\mathrm{H_2}}^{in,FR}$ $[mol/s]$
Value	16.6	0	0	0.12
Parameters	d_{AR} $[m]$	L_{AR} $[m]$	$F_{\mathrm{O_2}}^{in\ AR}[mol/s]$	$F_{\mathrm{N_2}}^{in\ AR}$ $[mol/s]$
Value	1.8	10	48.2	181.3

Axial profiles of the mean, bubble phase and emulsion phase species concentrations and of the volume fraction bubbles, emulsion gas and solids in the FR are shown in Figure 7. The methane conversion increases very fast in the first 0.5 to 1 m of the bed. Isothermal operation and chemical equilibrium limitations explain the observed profiles. With the inlet superficial gas velocity around 0.6 $[m_g^3/m_r^2 s]$, the bed voidage was around 0.65, much larger than the minimum fluidization voidage. The bed density is seen to decrease and then again increase from the inlet to outlet in the FR. This is the result of two phenomena, i.e. the gas volume expansion by the SMR reactions and the bubble rise velocity increase along the axial coordinate [59,61]. First, the SMR reactions are fast leading to an increasing bed voidage. As the reaction rates decrease while the bubble rise velocity keeps increasing, the bubble volume fraction decreases again. Bubble-emulsion phase mass transfer limitations are pronounced in the FR, especially under commercial conditions. It leads to species concentration in the emulsion phase very different from the mean and bubble phase species concentration. Some hydrogen is consumed by the reduction of NiO, resulting in an increase of the H_2O concentration. Although the catalytic activity of the OC is reduced by the presence of NiO, see the deactivation function, Eqs. (6) and (7), reforming rates are still high, even in the inlet region. This is also explained by low NiO content and low-pressure operation. A ~8% NiO concentration at the exit of AR is seen to have an overall minor effect on the reactor performance. The NiO concentration profile in the FR shows that the OC is nearly fully reduced. The pronounced solids dispersion in the commercial scale FR lowers the NiO concentration, especially in the bottom part of the FR where the OC returning from the AR is fed. The NiO concentration at the bottom of the FR is ~0.015 $[mol/kg_s]$, compared to ~0.49 $[mol/kg_s]$ at the outlet of the AR. This results in lower H_2O and CO_2 concentrations and higher methane concentrations in the emulsion phase and leads to an increased risk of coke formation.

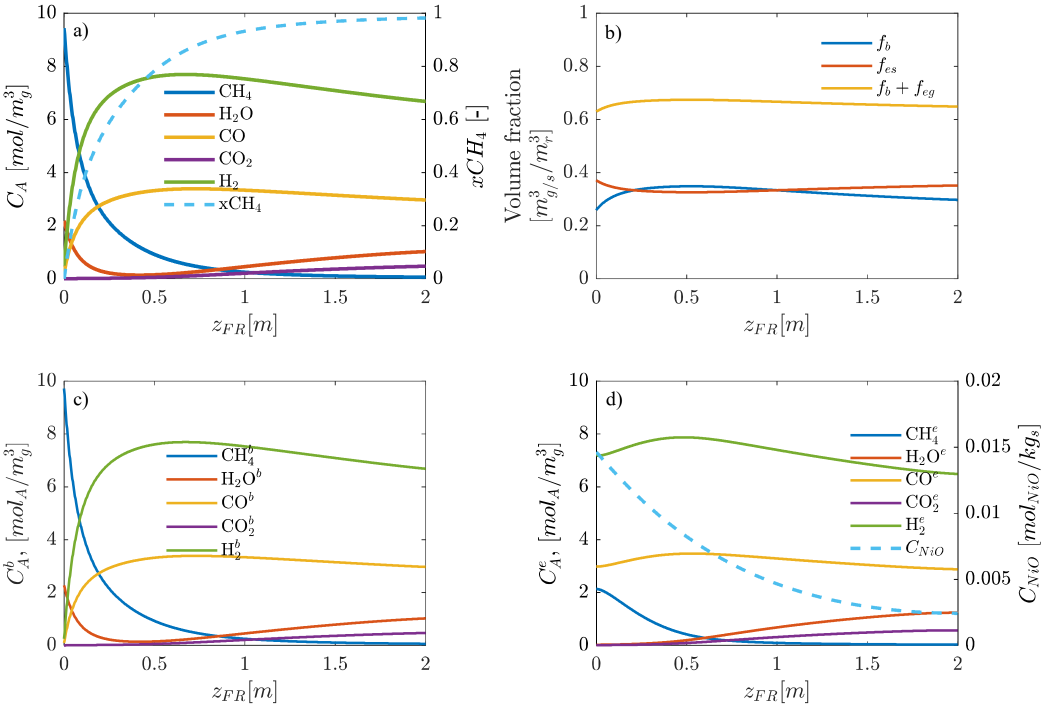

Figure 7. Axial profiles in the FR of a commercial scale a-CLR unit (a) mean species concentrations and methane conversion, (b) bubble, gas and solids volume fractions, (c) species concentrations in the bubble phase, (d) gas and solids species concentrations in the emulsion phase. Reference case reactor, dimensions and operating conditions (see Table 3).

Figure 8 summarizes the fluxes entering and leaving the AR and FR. It can be seen in Figure 8 that in the FR, the H_2O outlet flow rate is higher than the H_2O feed flow rate as a result of the reduction of NiO. The CO_2 outlet flow rate is also almost half of the outlet H_2O flow rate. In the reference case, the energy efficiency based on the lower heating value (LHV) estimated from the simulation is $\eta_e = LHV_{H_2+CO,out\ FR}/LHV_{CH_4,in\ FR} \cong 86\%$, which is theoretically competitive with SMR and POM/ATR. Various phenomena that can affect the energy efficiency are, however, not accounted for by lack of data on commercial scale a-CLR operation.

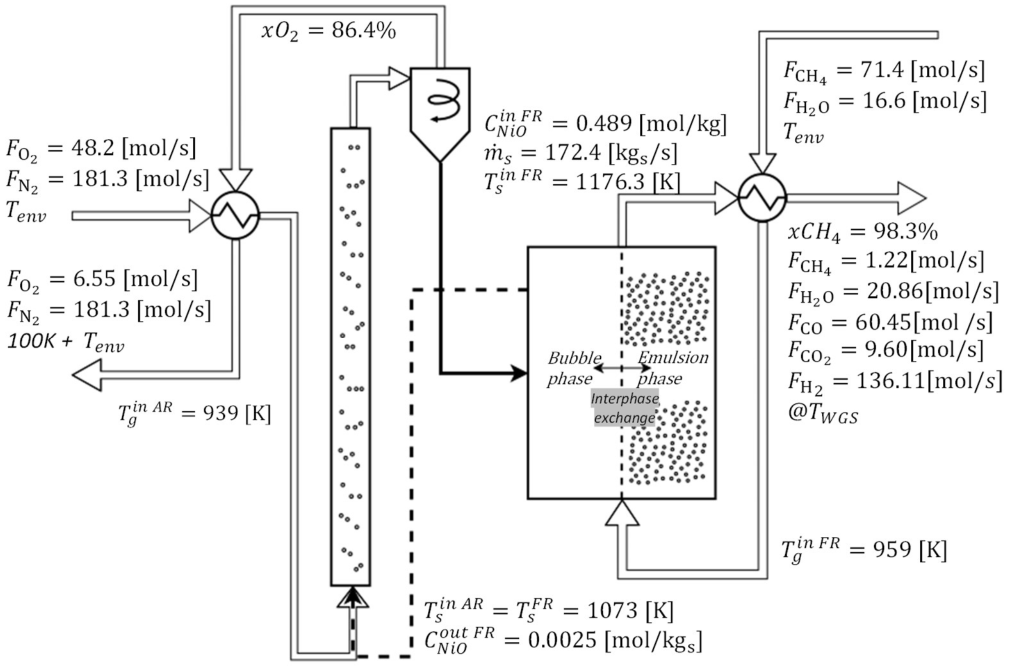

Figure 8. Simulated molar flow rate and conversions at the inlet and outlet of the AR and FR, and required solids circulation rate. Commercial scale a-CLR reference case (see Table 3).

Figure 9 shows the axial profiles of the reaction rates in the FR. The first steam methane reforming reaction is the fastest in the first 0.6 m of the bed, while the rates of the second SMR reaction and of NiO reduction by CH_4 are low. NiO is mainly reduced by hydrogen and CO. The rate of the reverse WGS reaction is almost equal to that of the CO reduction, indicating that the CO_2 formed by CO reduction is immediately consumed by the reverse WGS reaction, which is close to equilibrium at the simulated reaction conditions [55]. The a posteriori analysis of the risk of coke formation, as in Figure 9 right, shows that the Boudouard reaction and methane cracking tend to proceed forward in the first 0.5 m of the FR, so that coke formation is possible. Further downstream, coke formation by methane cracking is insignificant as a result of low methane and high hydrogen concentrations in the emulsion phase and the Boudouard reaction proceeds at high rate in the reverse direction, so that no net coke formation is expected. The eventual oxidation of coke by NiO is, however, not accounted for and may allow operating without the risk of coke formation in the bottom of the FR as well. Note that in the pilot scale tests reported in [28], the oxygen-to-methane feed ratio was higher as a result of heat losses and the low feed gas temperature, which results in lower methane concentration and higher H_2O and CO_2 concentrations in the emulsion gas compared to the commercial scale studied here.

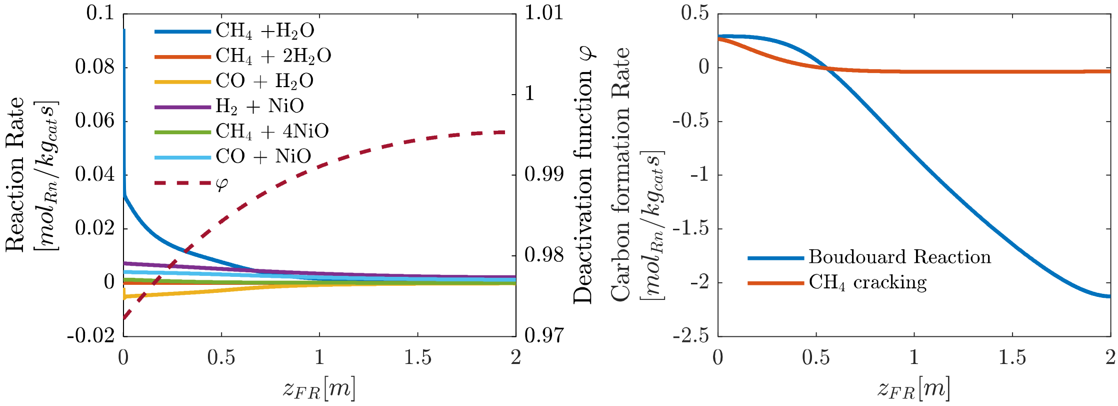

Figure 9. Axial profiles of the reaction rates in the FR. Left: Ni reduction and steam methane reforming. Right: Coke formation and gasification. Commercial scale a-CLR reference case (see Table 3).

Figure 10a shows axial profiles of the Ni and oxygen conversion in the AR. An exit Ni conversion of about 8% and oxygen conversion of about 86% are reached. This is explained by the large Ni-to-air feed ratio. Keeping the Ni conversion relatively low is important as the presence of NiO is detrimental for the catalytic activity in the FR. The solids residence time in the AR is about 2 s, with the air velocity exceeding 5 m/s as soon as the air reaches the solids temperature. The gas and solids temperature profiles are shown in Figure 10b. The gas temperature quickly approaches the temperature of the high heat capacity solids. With only 8% of Ni being oxidized in the AR, the increase of the solids temperature is about 100 K. The temperature increase has to be limited in order to prevent catalyst sintering and resulting deactivation, another reason for limiting the Ni conversion. A more pronounced temperature rise in the AR would also impose unrealistic tube material requirements. The maximum allowable temperature of UNS N06625, a widely used high temperature alloy for a-CLR units [75], is 982°C [76], which is about 80°C higher than the maximum temperature in the simulated AR. The solids circulation rate, as shown in Figure 8, is about 172 $[\mathrm{kg/s}]$, or about 66 $[\mathrm{kg}/m^2 s]$ that is a moderate value compared to reported solids circulation rates in other commercial processes [28,77,78].

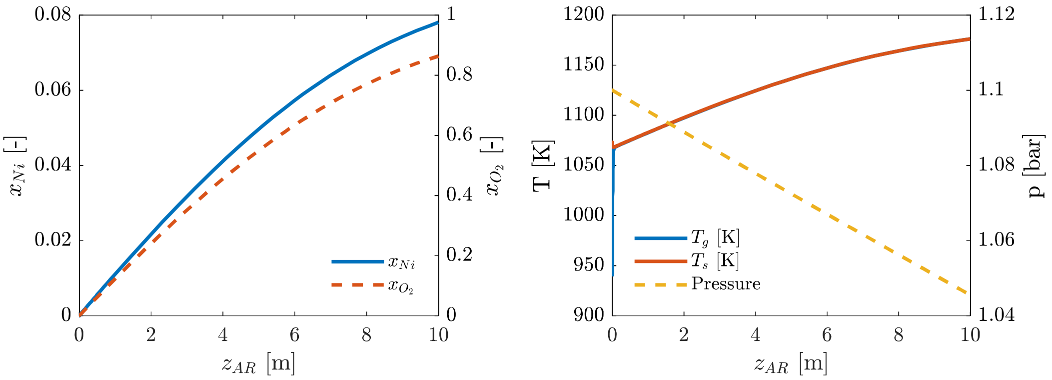

Figure 10. Axial profiles in the AR of the (left) Ni and O_2 conversion, (right) the gas and solids temperature and the total pressure. Commercial scale a-CLR reference case (see Table 3).

3.3 Influence the catalyst activity

The commercial scale reactor simulations can be used to guide OC/catalyst development. In this section, the influence of catalyst reactivity is investigated. The catalyst activity for the reforming reactions was multiplied with a factor of 10, 1, 0.1, 0.01, 0.001 and 0.0005, while keeping the NiO reduction rate and the Ni oxidation rate at the reference rates. Increasing the catalyst activity hardly improves the process performance. Only a strongly reduced catalyst activity, by a factor 100 or more, is seen to have some effect on the process performance. Intrinsic kinetics does not determine the FR performance at the reference activity. Bubble-emulsion phase mass transfer limitations are strong and the FR operates at a high catalyst-to-methane feed ratio. This finding also explains the minor effect of NiO on the reactor performance. The reactor performance cannot be directly linked to the catalyst activity.

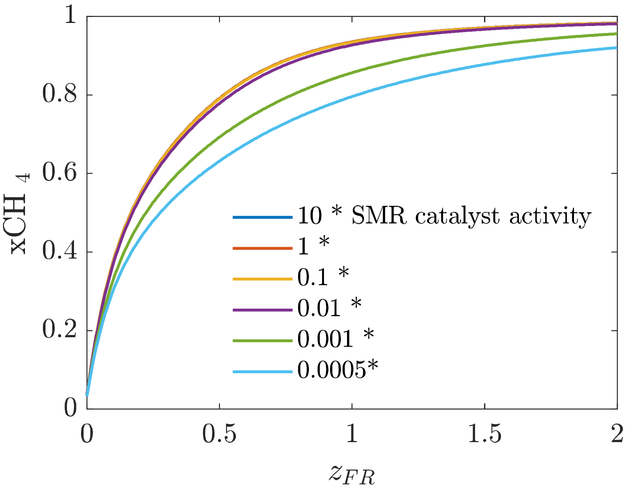

Figure 11. Influence of catalyst activity for the steam methane reforming on the methane conversion in the commercial scale FR. T_{FR} *= 1073K, FR inlet conditions: see Table 3.*

3.4 Influence of the main operating parameters

The influence of the FR operating temperature, the fuel feed rate, co-feeding CO_2 in the FR and the steam-to-methane feed ratio are investigated. The reactor dimensions were fixed to those used in the reference case. Two types of cases, marked as "$T_{p,out}$" (preheater outlet temperature) cases and "$T_{r,in}$" (reactor inlet temperature) cases, are discussed. The first type calculates the feed gas temperatures of the AR and FR with fixed exhaust temperatures for both pre-heaters. The second type imposes the feed gas temperatures of the AR and FR as 700K. The syngas yield, $(F_{\mathrm{H_2}}^{out} + F_{\mathrm{CO}}^{out})/(F_{\mathrm{CH_4}}^{in} xCH_4)$, is used to evaluate the energy efficiency of the a-CLR unit. The hydrogen yield, $F_{\mathrm{H_2}}^{out}/(F_{\mathrm{CH_4}}^{in} xCH_4)$, and the hydrogen to CO ratio, $F_{\mathrm{H_2}}^{out}/F_{\mathrm{CO}}^{out}$, are used to evaluate the property of the syngas.

3.4.1 Influence of the FR operating temperature

The operating temperature of the FR is an important parameter as it affects chemical equilibrium of the reactions as well as the reaction kinetics. It was varied between 973 and 1173K in this section. It should be noted that in the $T_{r,in}$ cases, the AR air feed rate had to be adjusted, i.e., increased to 6.82 $[\mathrm{kg/s}]$ at 1073K, to 7.03 $[\mathrm{kg/s}]$ at 1093K and 1113K, to 7.25 $[\mathrm{kg/s}]$ at 1133K and 1153K, and further increased to 7.47 $[\mathrm{kg/s}]$ at 1173K, in order to prevent depletion from oxygen in the AR. The fuel feed rate to the FR remained as in the reference case. Figure 12a confirms that the methane conversion increases when increasing the FR operating temperature and that the increase becomes less pronounced as the maximum possible methane conversion is approached. The methane conversion is seen to be higher in $T_{r,in}$ cases, especially at lower temperature, because of the higher NiO-to-CH_4 feed ratio, indicating that chemical equilibrium is the main limitation for converting CH_4 at lower temperature. The syngas ratio slightly increases with increasing FR temperature in the $T_{p,out}$ cases while it decreases in the $T_{r,in}$ cases. For the $T_{r,in}$ cases, extra heat is needed to heat the feed gas to the FR temperature, heat that is originally generated in the AR by oxidizing the Ni, so that also more NiO needs to be reduced in the FR. This leads to a higher fraction of the CH_4 being fully oxidized and a lower syngas ratio. In the $T_{p,out}$ cases, the difference between the FR operating temperature and the imposed exhaust gas temperature of the pre-heater increases when the FR temperature increases. This increases the amount of FR feed gas pre-heating, narrowing the difference between the FR feed gas temperature and the FR operating temperature. Thus, less CH_4 needs to be completely oxidized, leading to a slightly higher syngas ratio. As seen in As expected, the O_2 conversion increases with increasing FR temperature or methane conversion, as seen in Figure 12b. Figure 12c confirms that the NiO-to-methane feed ratio increases with increasing FR temperature in the $T_{r,in}$ cases, while slightly decreases in the $T_{p,out,}$ cases. Although the air feed rate had to be increased for the four highest FR temperatures in the $T_{r,in}$ cases, the overall increasing trend of the NiO-to-methane feed ratio is clear. It is worth noting that the FR feed gas temperature increases to 1100K when the FR operating temperature increases in the $T_{p,out}$ cases, which may not be realistic in practice. The hydrogen yield and H_2/CO-ratio both decrease with increasing FR temperature because the WGS reaction is shifted to the left at higher FR temperature.

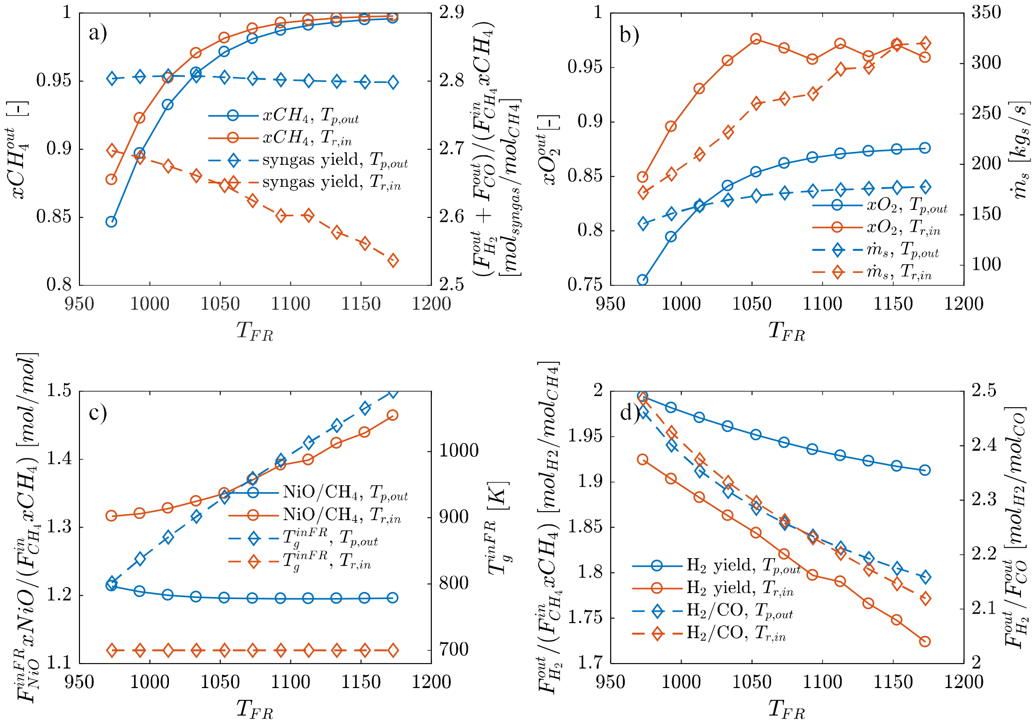

Figure 12. Influence of the FR operating temperature. The blue lines indicate the $T_{p,out}$ cases, the red lines the $T_{r,in}$ cases. Solid lines refer to the left axis, dashed lines to the right axis. Other simulation conditions as in the commercial scale reference case (Table 3).

3.4.2 Influence of the fuel feed rate

The influence of the fuel feed rate was studied with the FR operated at 1073K. The fuel feed rate is expressed in number of equivalent conventional steam reformer tubes and was varied between 46 and 54, while the steam-to-methane feed ratio remained 0.23. To prevent oxygen depletion in the AR, the AR air feed rate was increased to 6.82 $[\mathrm{kg/s}]$ for the $T_{r,in}$ cases at an equivalent number of tubes of 50, to 7.03 $[\mathrm{kg/s}]$ for that of 52, and to 7.25 $[\mathrm{kg/s}]$for that of 54. As seen in Figure 13a, the methane conversion slightly decreases with increasing fuel feed rate, whereas the syngas ratio is nearly constant. With the FR diameter fixed, the added fuel enters the bubble phase and its reaction requires exchange with the emulsion phase. Although $T_{r,in}$ cases show a higher methane conversion, the syngas yield is reduced as a result of the lower gas inlet temperature that requires more CH_4 to be fully oxidized. Figure 13b shows that with increasing fuel feed rate, both the solids circulation rate and the O_2 conversion increase significantly as more feed gas has to be heated and converted, requiring more heat to be generated from the oxidation of Ni in the AR. The NiO-to-CH_4 feed ratio remains almost unchanged in the $T_{p,out}$ cases, while in the $T_{r,in}$ cases, it is seen to decrease slightly with increasing fuel feed rate. This is because the heat losses via the AR outlet gas decrease when the O_2 conversion increases. As the FR operating temperature and the feed H_2O/CH_4-ratio were fixed, the hydrogen yield and H_2/CO-ratio remain almost unchanged. For the H_2/CO-ratio, the very small difference between the $T_{p,out}$ and $T_{r,in}$ cases is mainly due to the equilibrium shift of the WGS reaction caused by the H_2O and CO_2 from full oxidation of CH_4. Whereas both $T_{r,in}$ and $T_{p,out}$ cases show similar trends, the $T_{r,in}$ cases offer a higher CH_4 conversion but require more oxygen to be transported from the AR to the FR to ensure autothermal operation.

This leads to a lower syngas production and hydrogen yield, as well as higher NiO-to-CH_4 feed ratio and solids circulation rate.

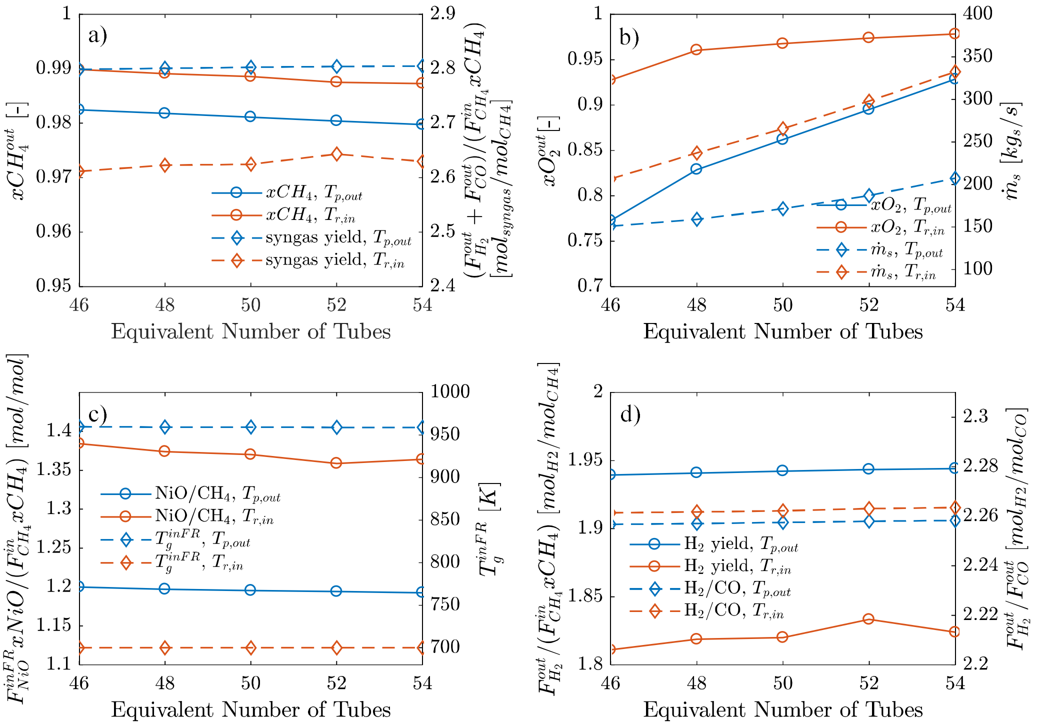

Figure 13. Influence of fuel feed rate. The blue lines indicate the $T_{p,out}$ cases, the red lines the $T_{r,in}$ cases. Solid lines refer to the left axis, dashed lines to the right axis. Other simulation conditions as in the commercial scale reference case (Table 3).

3.4.3 Influence of co-feeding CO_2 to the FR

The influence of co-feeding CO_2 with H_2O in the FR was studied, keeping the $(H_2O+CO_2)/CH_4$ feed ratio at 0.23. The CH_4 feed rate and the FR operating temperature were the same as in the reference case, but the air feed was increased to 6.82 [kg/s] for the initial five $CO_2/(H_2O+CO_2)$ ratios, i.e. for $CO_2/(H_2O+CO_2)$ = 0-0.8, and increased further to 7.03 [kg/s] when CO_2 fully replaced H_2O in the $T_{r,in}$ cases.

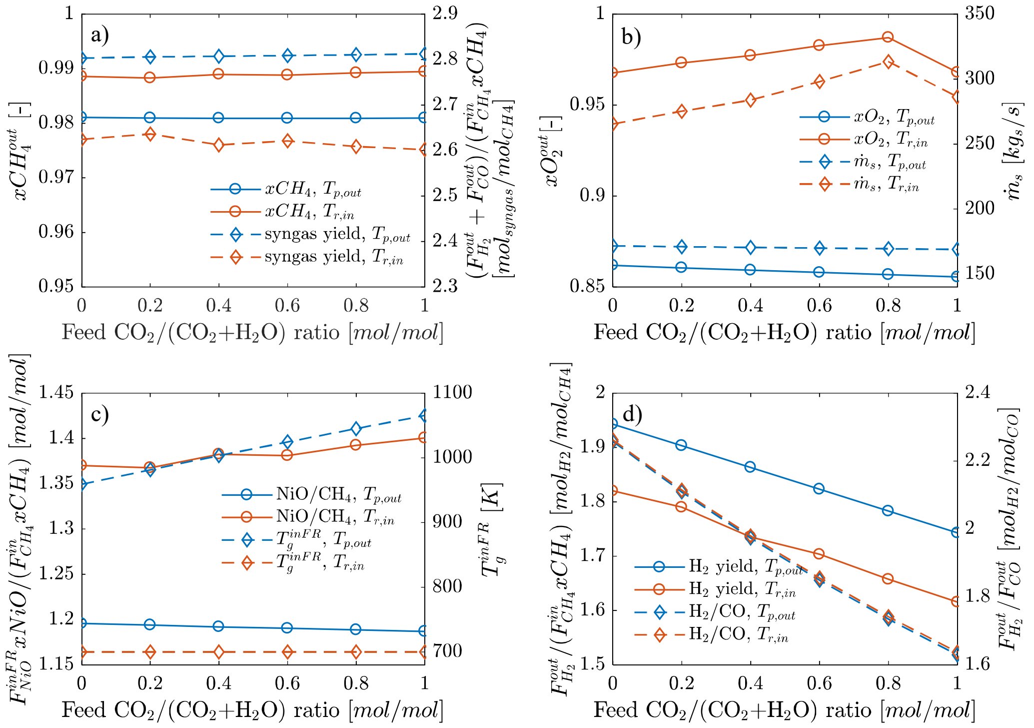

Figure 14. Influence of the $CO_2/(CO_2+H_2O)$ feed ratio, the $(CO_2+H_2O)/CH_4$ feed ratio was 0.23. The blue lines indicate the $T_{p,out}$ cases, the red lines the $T_{r,in}$ cases. Solid lines refer to the left axis, dashed lines to the right axis. Other simulation conditions as in the commercial scale reference case (Table 3).

Figure 14a shows that the methane conversion remains almost unchanged with increasing CO_2/CH_4 feed ratio. When co-feeding CO_2, the syngas yield decreases slightly in the $T_{r,in}$ cases because of increased full oxidation of methane needs for CO_2 reforming, while it remains unchanged in the $T_{p,out}$ cases because the increase of the gas feed temperature somewhat compensates the energy consumption. For the same reason, the O_2 conversion also slightly increases (Figure 14b) in the $T_{r,in}$ cases. The O_2 conversion decreasing in the $T_{p,out}$ cases is mainly a result of the increasing fuel feed temperature and related lower energy needs to maintain autothermal operation. It also results in a higher syngas yield than in the $T_{r,in}$ cases. As seen in Figure 14c, the calculated FR gas inlet temperature increases to above 1050 K in the

$T_{p,out}$ cases at high $CO_2/(H_2O+CO_2)$ feed ratio, because less heat is needed to evaporate H_2O with increasing $CO_2/(H_2O+CO_2)$ feed ratio. Figure 14d confirms that both the hydrogen yield and H_2/CO-ratio decrease significantly when increasing the $CO_2/(H_2O+CO_2)$ feed ratio, as expected from the stoichiometry of the steam and CO_2 reforming reactions and the shift of the chemical equilibrium of the WGS reaction. Like the syngas yield, the hydrogen yield is higher in the $T_{p,out}$ cases. The H_2/CO-ratio is much less affected by the NiO-to-CH_4 feed ratio than by the $CO_2/(CO_2+H_2O)$ feed ratio.

Figure 15 shows the axial profiles of the mean and emulsion phase species concentrations and of the reaction rates in the FR for the dry-CLR reforming case ($CO_2/(H_2O+CO_2)$ ratio = 1). The CO concentration is seen to be significantly higher than that in the reference case, while the methane conversion and NiO concentration are similar. It is seen that the rate of the reverse WGS reaction is relatively high in the first meter of the FR, producing H_2O that allows the SMR reactions to proceed. Although dry reforming is not explicitly listed in the global reactions taken into account, dry reforming is seen to proceed through a combination of the reverse WGS and first SMR reaction. Because of the high CO and CH_4 concentrations in the emulsion gas, coke formation can be expected in the first 0.5 m of the FR as a result of methane cracking and the Boudouard reaction, while in the upper part of the FR the WGS reaction and reverse Boudouard reaction eliminate the risk of coke formation (Figure 15d). The potential oxidation of coke by NiO in the first meter of the FR was not taken into account in this work. Co-feeding CO_2 in a-CLR for optimizing the H_2/CO-ratio for methanol or Fishes-Tropsch synthesis is, therefore, an option that needs further analysis and catalyst development.

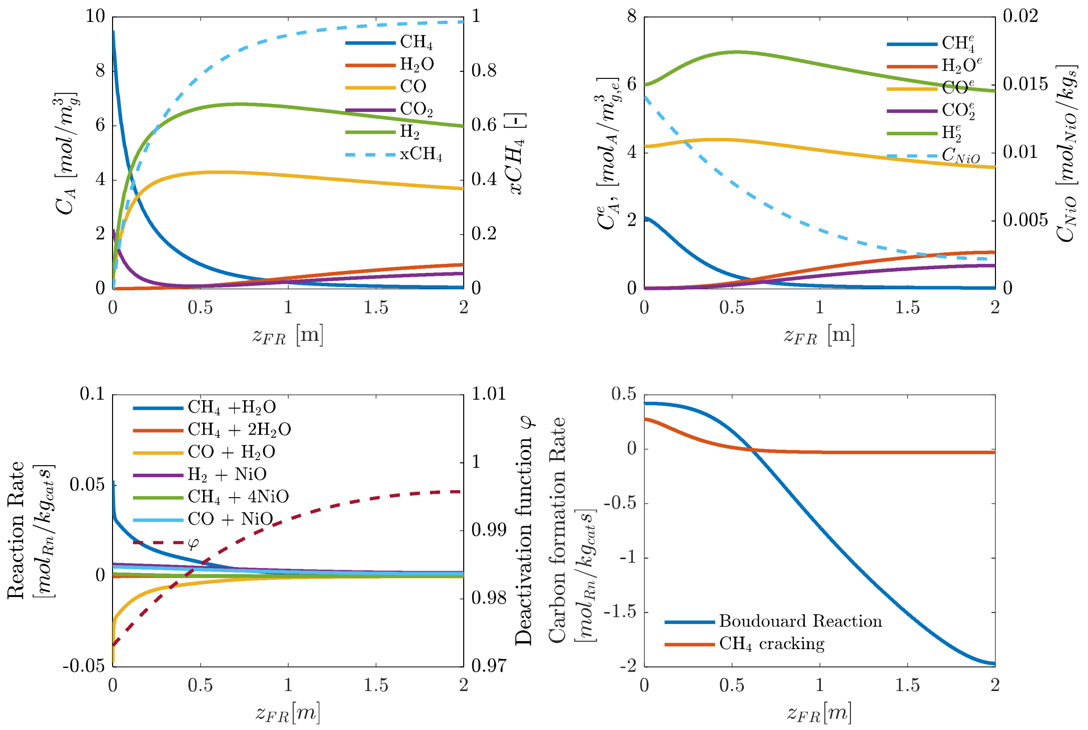

Figure 15. Axial profiles in FR of the of the a) mean species concentrations and methane conversion, b) species concentration in the emulsion phase, c) reaction rate profiles and d) coke formation risk analysis. Case study with feed $CO_2/(H_2O+CO_2)=1$. Other simulation conditions as in the commercial scale reference case (Table 3).

3.4.4 Influence of the steam-to-methane feed ratio

Previous CLR experiments [28,30] showed the a-CLR unit could operate at steam-to-methane feed ratios of 0-0.5, although autothermal operation could not be ensured. In the present work, autothermal conditions were determined while the steam-to-methane feed ratio was varied from 0.1 to 0.5, keeping the FR operating temperature, and the methane feed rate as in the reference case, but increasing the air feed rate to 6.82 [kg/s] in the $T_{r,in}$ cases. As seen in Figure 16a, with increasing steam flow rate, the methane conversion slightly increases, as excess steam has a positive effect on the SMR reaction thermodynamics and kinetics, but reduces the space time in the reactor and increases the fraction of gas in the bubble phase. The observed reaction rates are not only determined by bubble-emulsion phase mass transfer, but also by chemical equilibrium. The syngas yield, on the other hand, continuously decreases as more CH_4 is fully oxidized as excess steam needs to be heated up. For reasons explained previously, the $T_{r,in}$ cases exhibit a higher methane conversion, whereas the $T_{p,out}$ cases exhibit a higher syngas yield.

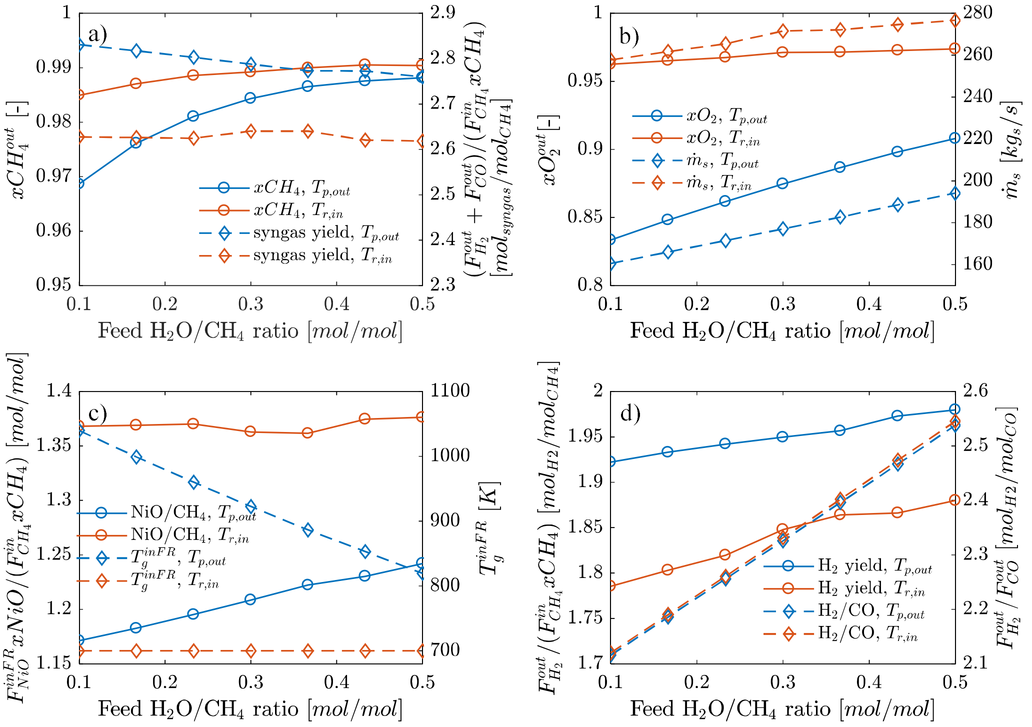

Figure 16. Influence of the feed H_2O/CH_4-ratio. The blue lines indicate the $T_{p,out}$ cases, the orange lines the $T_{r,in}$ cases. Solid lines refer to the left axis and dashed lines to the right axis. Other simulation conditions as in the commercial scale reference case (Table 3).

As seen in Figures 16b and 16c, a larger fraction of the feed CH_4 being fully oxidized with increasing steam flow rate being heated up to the desired FR temperature is reflected in an increase of the O_2 conversion and of the solids circulation rate, in particular in the $T_{p,out}$ cases. The NiO-to-CH_4 feed ratio then also increases although the methane conversion also determines the energy requirement in the FR. In the $T_{p,out}$ cases, the gas inlet temperature decreases with increasing H_2O-to-CH_4 feed ratio, as seen in Figure 16c, which results in a further increased energy requirement. This explains the more pronounced effect of the steam flow rate on the O_2 conversion and on the NiO-to-CH_4 feed ratio. Figure 16d shows that, as expected, with increasing steam flow rate, the hydrogen yield as well as the H_2/CO-ratio increases ratio in both cases as a result of the shift in equilibrium of the SMR and WGS reactions. Finally, it is seen that a higher gas inlet temperature always results in an increased syngas yield and lower O_2 conversion. The simulation confirms the importance of utilizing the energy in the off-gas for pre-heating the feed gas of the AR and FR.

3.5 The solids circulation rate

A major question is whether the solids circulation rate can be kept at realistic values. For various circulating and dual fluidized bed applications, solids circulation rates of 400 to 600 $\mathrm{kg_s}/s$ and of up to $600\ [\mathrm{kg_s}/m_r^2 s]$ have been reported [79]. In the field of a-CLR, Abad et al. [50] reported a solids circulation rate of 80 $[\mathrm{kg_s}/m_r^2 s]$, and Pröll et al. [28] of 20-100 $[\mathrm{kg_s}/m_r^2 s]$ with the AR exit superficial velocity 3-8 $[m_g^3/m_r^2 s]$. The simulations in the present work show that, to ensure autothermal operation in a 50-tube equivalent commercial a-CLR unit, the calculated solids circulation rates vary from about 150 $[\mathrm{kg}/s]$ to 300 $[\mathrm{kg}/s]$, corresponding to 59-118 $[\mathrm{kg_s}/m_r^2 s]$, so within the ranges technically feasible and with commercially acceptable reactor dimensions and conversions. The AR exit superficial gas velocity is about $5\ [m_g^3/m_r^2 s]$.

For given methane conversion, the required solids circulation rate depends on the Ni conversion and the amount of oxygen to be transported from the AR to the FR to ensure autothermal operation. Of the various operating parameters, the gas feed temperature is seen to have the most significant effect on the required oxygen. The mean difference between the feed gas temperature in $T_{p,out}$ and $T_{r,in}$ cases is defined as (the feed gas temperature in $T_{r,in}$ cases is fixed 700 K):

$$\Delta T_g^{in} = 0.5\left(T_g^{in\,FR}|_{T_{p,out}\,case} - 700 + T_g^{in\,AR}|_{T_{p,out}\,case} - 700\right) \tag{39}$$

The difference between required oxygen to convert CH_4 ratio in the $T_{r,in}$ and $T_{p,out}$ cases can be defined by the difference of the ratio $\dot{m}_s\left(C_{NiO}^{in\,FR} - C_{NiO}^{out\,FR}\right)/F_{CH_4}^{in\,FR}xCH_4$ in $T_{r,in}$ and $T_{p,out}$ cases. It is seen in Figure 17 that increasing the feed gas temperature to both the AR and FR by 100 K results in a decrease of required oxygen to converted CH_4 by about by 0.0662 (or about 5%), which affects the syngas yield and solids circulation rate.

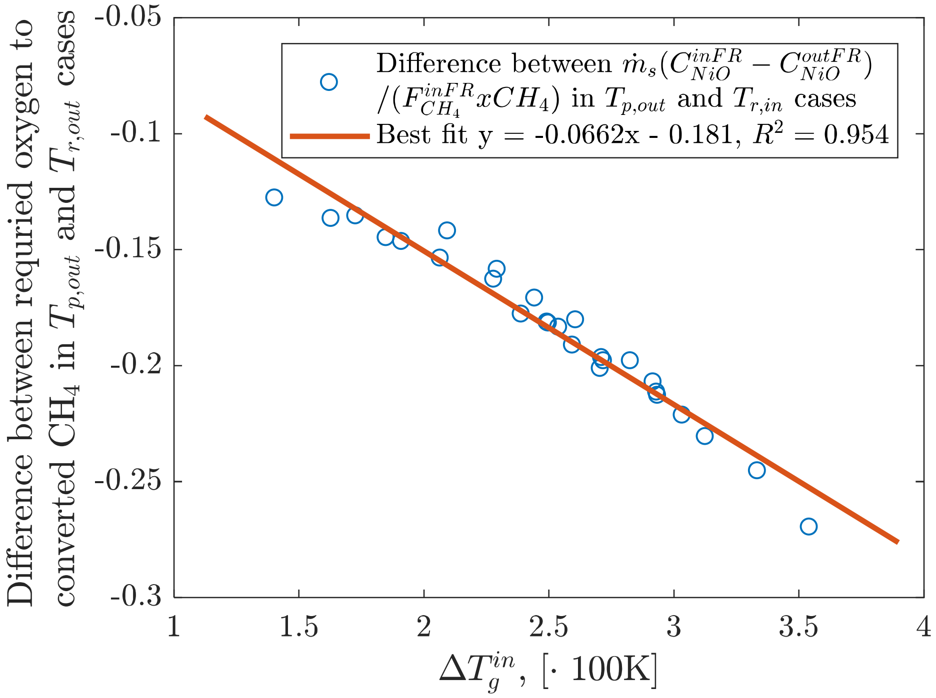

Figure 17. Difference between required oxygen to converted-CH_4 ratio in $T_{p,out}$ and $T_{r,in}$ cases vs. mean difference between inlet gas temperatures in $T_{p,out}$ and $T_{r,in}$ cases. Operation conditions as in section 3.4. Data: see Figure 13c, Figure 14c and Figure 16c.

For a given oxygen requirement, the more Ni is converted in the AR, the lower the required solids circulation rate. The Ni conversion in the AR has to be limited, however, as it can cause excessive temperature rise in the AR, thereby increasing the risk of OC sintering and deactivation. Furthermore, NiO formation causes strong deactivation of the catalyst for the SMR and WGS reactions in the FR. Because of the relatively high OC reactivity considered in the present work, the height of the AR was limited to 5 m, but this height can be increased when using a less active OC.

4 Conclusions

A detailed simulation model for a-CLR was developed to evaluate the feasibility of a-CLR at commercial scale. It accounts for essential phenomena of fluidized bed hydrodynamics and detailed reaction kinetics. The model was validated using published pilot plant data and then used to study a commercial scale a-CLR design with a capacity equivalent to 50 conventional SMR tubes. A commercial scale a-CLR design with a 4 m diameter, 2 m tall FR and a 1.8 m diameter, 10 m tall AR was selected after simulating the FR and the AR with different feed gas velocities and considering the need for a high methane conversion in an as compact as possible FR, a realistic solids circulating rate and an appropriate temperature rise in the AR. The simulations show that the a-CLR unit can achieve autothermal operation with 98% methane conversion when its FR is operated at 1073K with a 0.23 steam-to-methane feed ratio and 86% O_2 conversion with a solids circulation rate of 172 $[\mathrm{kg_s/s}]$. The low Ni oxidation state in both the FR and the AR distinguishes CLR from CLC, with NiO being nearly fully reduced in the FR. The catalytic activity of the OC is seen to have a small influence on the methane conversion due to high solids-to-gas feed ratio in the FR and the dominant bubble-emulsion phase mass transfer limitations. The influence of different operating parameters was also studied. The methane conversion was found to be sensitive to the FR operating temperature below 1073K. The steam-to-methane feed ratio affects the methane conversion through the chemical equilibrium and kinetics and via the mass transfer between the bubble and emulsion phase. Co-feeding CO_2 into the FR can be considered to adjust the H_2/CO-ratio of the syngas, but a risk of coke formation in the bottom of the FR exists, although the potential oxidation of the coke by the NiO requires further investigation. The required oxygen transport from the AR to the FR to ensure autothermal operation was found to depend on the fuel inlet temperature, the steam-to-methane feed ratio and the eventual co-feeding of CO_2. Simulations with fixed feed gas temperatures and with fixed exit temperature of heat exchangers used to preheat the feed gases show that utilizing the off-gas from both the AR and the FR to preheat the feed gas to the AR and FR improves the syngas yield and decreases the required oxygen transport from the AR to the FR. The required NiO-to-CH_4 feed ratio for autothermal operation ranges from 1.1 to 1.4 depending on the other operating parameters, while increasing the feed gas temperature in both AR and FR by 100 K reduces the required NiO-to-CH_4 feed ratio by about 0.0662.

Acknowledgement

The authors gratefully acknowledge the financial support from the FNRS (Fonds de la Recherche Scientifique) project (T.0230.16) and from CSC (China Scholarships Council) to Zirui He (No. 201606220058). The authors also want to thank Professor Tobias Pröll from Universität für Bodenkultur Wien for the discussion on the validation case used in this work.

Appendix A. Thermodynamic and rate constants for the reaction model, constitutive equations and boundary conditions for the reactor hydrodynamic model

Table A. 1 Thermodynamic and rate constants.

Note:	The reaction rate constants, equilibrium constant and adsorption constants are calculated using Arrhenius/van't Hoff expressions except if otherwise specified: $k_j = A_j \exp\left(-\frac{E_{a,j}}{RT}\right)$ $K_j = A_j \exp\left(-\frac{E_{a,j}}{RT}\right)$ $K_A = \hat{A}_A \exp\left(-\frac{\Delta H_A^a}{RT}\right)$		
AR [35]	A_{R1}	1.56×10^{-3}	$[kg_s/mol \cdot s]$
	$E_{a,R1}$	31.15	$[kJ/mol]$
	$\hat{A}_{O_2}$	31.5	$[bar^{-1}]$
	$\Delta H_{O_2}^a$	-28.27	$[kJ/mol]$
FR adapted from [50,51,56,57]	A_{R2}	0.151	$[mol^{-n_{Red}} \cdot m^{-3n_{Red}}]$
	A_{R3}	50.0	
	A_{R4}	0.084	
	$E_{a,R2}$	78	$[kJ/mol]$
	$E_{a,R3}$	26	
	$E_{a,R4}$	25	
	n_{R2}	0.8	[-]
	n_{R3}	0.5	
	n_{R4}	0.8	

A_{R5}	1.174×10^{15}	$[mol \cdot bar^{0.5}/kg_s \cdot s]$
A_{R6}	5.430×10^{5}	$[mol\ /kg_s s]$
A_{R7}	2.833×10^{14}	$[mol \cdot bar^{0.5}/kg_s \cdot s]$
$E_{a,R5}$	240.1	$[kJ/mol]]$
$E_{a,R6}$	67.13	
$E_{a,R7}$	243.9	
$K_j = 10^{\frac{B_j}{T}+C_j}, j = R5, R6, R7$		
B_{R5}	-11650	$[K]$
B_{R6}	-9740	
B_{R7}	1910	
C_{R6}	13.706	[-]
C_{R6}	-1.764	
C_{R7}	11.312	
$\hat{A}_{CO}$	8.23×10^{-5}	$[bar^{-1}]$
$\hat{A}_{H_2}$	6.12×10^{-9}	
$\hat{A}_{CH_4}$	6.65×10^{-4}	
$\hat{A}_{H_2O}$	1.77×10^{5}	[-]
ΔH^a_{CO}	-70.65	$[kJ/mol]$
$\Delta H^a_{H_2}$	-82.90	
$\Delta H^a_{CH_4}$	-38.28	
$\Delta H^a_{H_2O}$	88.86	
A_{kB}	7.43×10^{6}	$[mol\ /kg_s s]$
$\hat{A}_{KCO}$	1.025×10^{-6}	$[bar^{-1}]$
$\hat{A}_{KO,CO2}$	30.2×10^{6}	$[bar]$
E_{kB}	108.38	$[kJ/mol]$

	ΔH^{a}_{KCO}	-92.543	
	$\Delta H^{a}_{KO,CO2}$	89.80	
	A_{KB}	1.25×10^{-9}	$[bar^{-1}]$
	A_{kCrk}	65×10^{3}	$[mol\ /kg_{s}s]$
	$\hat{A}_{KCH4}$	0.21	$[bar^{-1}]$
	$\hat{A}_{K''r}$	30.2×10^{6}	$[bar^{1.5}]$
	A_{KCrk}	1.16×10^{6}	$[bar]$
	E_{KB}	-162.48	$[kJ/mol]$
	E_{kCrk}	59.03	
	ΔH^{a}_{KCH4}	0.143	
	$\Delta H^{a}_{K''r}$	89.805	
	E_{KCrk}	100.765	

Table A. 2. Constitutive equations

AR &FR	$u_t = \sqrt{4gd_p\left(\rho_s - \rho_g^{in\ AR}\right) \Big/ 3\rho_{g0}C_D}$ [37]
	$Re_p = \rho_g u_t d_p \mu^{-1}$
	$C_D = \begin{cases} 24Re_p^{-1} & \left(Re_p < 0.4\right) \\ 10Re_p^{-0.5} & \left(0.4 \leq Re_p < 500\right) \end{cases}$ [37]
	$u_{mf} = 1.118 * 10^{-13}\left(d_p * 10^6\right)^{1.82}\left(\rho_s - \rho_g\right)^{0.94} \Big/ \rho_g^{0.06}\mu^{0.88}$ [80]
AR	$u_{sg} = \frac{RT}{p}\hat{F}_{\text{tot}}, (\hat{F}_{\text{tot}} = \hat{F}_{O_2} + \hat{F}_{N_2})$
	$u_{ss} = \frac{\dot{m}_s}{\rho_s \Omega}$
	$\varepsilon_g = 0.5\left[\left(u_{sg} + u_t + u_{ss}\right) - \left(\left(u_{sg} + u_t + u_{ss}\right)^2 - 4u_{sg}u_t\right)^{0.5}\right]u_t^{-1}$ [37]
	$a_v = 6\left(1 - \varepsilon_g\right)d_p^{-1}$
	$j_D = j_H = 2.06Re_p^{-0.575}\varepsilon_g^{-1}$
	$k_g = j_D u_{sg}\rho_g Sc^{-\frac{2}{3}}\left(M_{O_2}p_{fO_2}\right)^{-1}$ [37,81]
	$h_f = j_H C_{p,g}u_{sg}\rho_g Pr^{-\frac{2}{3}}$ [37]
	$\eta_s = 0.05\left(1 - \varepsilon_g\right)u_{ss}^{-1}$
	$\eta_g = \begin{cases} 0.0791Re_t^{-0.25} & (3 \times 10^3 < Re_t \leq 10^5) \\ 0.0008 + 0.0552Re_t^{-0.237} & (10^5 < Re_t \leq 10^8) \\ 0\ (else) & \end{cases}$ [60]
	$Re_t = d_t u_{sg}\rho_g \mu^{-1}$
FR	$\Delta F_{A,Ei} = C_{Ae}\frac{\sum r_A \rho_s f_{es}}{\sum C_{Ae}}$
	$f_b u_b = \frac{RT_{FR}}{p(z)}\sum \hat{F}_{Ab}$
	$f_{eg}u_{eg} = \frac{RT_{FR}}{p(z)}\sum \hat{F}_{Ae}$
	$u_{sg} = f_b u_b + f_{eg}u_{eg} = f_b u_b + u_{mf}$

	$f_b(z) = \left[u_{sg}(z) - u_{mf}\right]/u_b(z)$
	$u_b = u_{sg} - u_{mf} + \Psi(g d_b)^{0.5}$ [70] $\Psi = 0.64$, for $\mathrm{d_t} < 0.1\ m$, $\Psi = 1.6\mathrm{d_t^{0.4}}$, for $0.1 < d_t < 1\ m$, $\Psi = 1.6$ for $\mathrm{d_t} > 1\ m$. [71] $\frac{d_{bm} - d_b(z)}{d_{bm} - d_{b0}} = \exp\left(-\frac{0.3z}{d_t}\right)$ [68] $d_{b0} = 0.376\left(u_{sg} - u_{mf}\right)^2$ [68] $d_{bm} = 1.638\left[0.25\pi d_t^2\left(u_{sg} - u_{mf}\right)\right]^{0.4}$ [67]
	$k_I = f_b \frac{10.4 u_{sg}}{\pi d_b}$ [66]
	$D_{es} = \begin{cases} 0.06 + 0.1u_{sg},\ Small\ reactor \\ 0.3d_t^{0.65},\ Large\ reactor \end{cases}$ [59]
	$u_{sp} = \frac{\dot{m}_s}{f_{es}\rho_s\Omega}$
	$f_{es} = 1 - \varepsilon_{mf}(1 - f_b)$ [59]

Table A. 3. Boundary conditions

AR	$\hat{F}_{O_2}^{in\ AR} = 0.21 \cdot G_{\mathrm{g}}^{in\ AR}/\Omega_{AR} M_{O_2}$
	$C_{O_2}^{s,0} = 0$
	$C_{Ni}^{in\ AR} = C_{Ni}^{out\ FR}$
	$T^0 = T_g^{in\ AR}$
	$T_s^0 = T_s^{in\ AR} = T_{FR}$
	$p_{tot}^0 = p^0$
FR	$\hat{F}_{Ab}(0^+) = C_{Ab}^0 \cdot f_b^0 u_b^0$
	$\hat{F}_{Ae}(0^+) = f_{eg}^0 u_{eg}^0 C_{Ae}^0 + \frac{D_{eg}}{f_{eg}^0 u_{eg}^0}\frac{\partial \hat{F}_{Ae}}{\partial z}(0^+)$

	$C_{NiO}(0^+) = C_{NiO}^{out\ \mathrm{AR}} + \frac{D_{es}}{u_{sp}^0}\frac{\partial C_{NiO}}{\partial z}(0^+)$
	$f_b^0 = \frac{u_{sg}^0 - u_{mf}}{u_b^0 - u_{mf}}$
	$\frac{D_{eg}}{f_{eg}u_{eg}}\frac{\partial F_{Ae}}{\partial z}(H^-) = 0$
	$\frac{D_{es}}{u_{sp}}\frac{\partial C_{NiO}}{\partial z}(H^-) = 0$

References

[1] J.R. Rostrup-Nielsen, Syngas in perspective, Catalysis Today 71 (2002) 243–247. https://doi.org/10.1016/S0920-5861(01)00454-0.

[2] S.A. Ghoneim, R.A. El-Salamony, S.A. El-Temtamy, Review on Innovative Catalytic Reforming of Natural Gas to Syngas, World Journal of Engineering and Technology 04 (2016) 116–139. https://doi.org/10.4236/wjet.2016.41011.

[3] R. Soltani, M.A. Rosen, I. Dincer, Assessment of CO2 capture options from various points in steam methane reforming for hydrogen production, International Journal of Hydrogen Energy 39 (2014) 20266–20275. https://doi.org/10.1016/j.ijhydene.2014.09.161.

[4] A.M. De Groote, G.F. Froment, Simulation of the catalytic partial oxidation of methane to synthesis gas, Applied Catalysis A: General 138 (1996) 245–264. https://doi.org/10.1016/0926-860X(95)00299-5.

[5] M.A. Pen˜a, J.P. Gómez, J.L.G. Fierro, New catalytic routes for syngas and hydrogen production, Applied Catalysis A: General 144 (1996) 7–57. https://doi.org/10.1016/0926-860X(96)00108-1.

[6] S.A. Al-Sayari, Recent Developments in the Partial Oxidation of Methane to Syngas, TOCATJ 6 (2013) 17–28. https://doi.org/10.2174/1876214X20130729001.

[7] C. Alvarez-Galvan, M. Melian, L. Ruiz-Matas, J.L. Eslava, R.M. Navarro, M. Ahmadi, B. Roldan Cuenya, J.L.G. Fierro, Partial Oxidation of Methane to Syngas Over Nickel-Based Catalysts: Influence of Support Type, Addition of Rhodium, and Preparation Method, Front. Chem. 7 (2019) 104. https://doi.org/10.3389/fchem.2019.00104.

[8] P. Chiesa, Advanced technologies for syngas and hydrogen (H 2) production from fossil-fuel feedstocks in power plants, in: D. Roddy (Ed.), Advanced power plant materials, design and technology, Woodhead Pub. Ltd, Cambridge, UK, 2010, pp. 383–411.

[9] Ana-Maria Cormos, Szabolcs Szima, Szabolcs Fogarasi, Calin-Cristian Cormos, Economic Assessments of Hydrogen Production Processes Based on Natural Gas Reforming with Carbon Capture, Chemical Engineering Transactions 70 (2018) 1231–1236. https://doi.org/10.3303/CET1870206.

[10] B. Sørensen, Hydrogen and fuel cells: Emerging technologies and applications / Bent Sørensen, secondnd ed., Academic Press, Oxford, Burlington, MA, 2012.

[11] C.M. Kalamaras, A.M. Efstathiou, Hydrogen Production Technologies: Current State and Future Developments, Conference Papers in Energy 2013 (2013) 1–9. https://doi.org/10.1155/2013/690627.

[12] T. Mattisson, A. Lyngfelt, Applications of chemical-looping combustion with capture of CO2, Second Nordic Minisymposium on CO2 Capture and Storage, Göteborg, Sweden (2001).

[13] R.K. Lyon, J.A. Cole, Unmixed combustion: an alternative to fire, Combustion and Flame 121 (2000) 249–261. https://doi.org/10.1016/S0010-2180(99)00136-4.

[14] M. Tang, L. Xu, M. Fan, Progress in oxygen carrier development of methane-based chemical-looping reforming: A review, Applied Energy 151 (2015) 143–156. https://doi.org/10.1016/j.apenergy.2015.04.017.

[15] A. Abad, A. Cabello, P. Gayán, F. García-Labiano, L.F. de Diego, T. Mendiara, J. Adánez, Kinetics of CaMn0.775Ti0.125Mg0.1O2.9-δ perovskite prepared at industrial scale and its implication on the performance of chemical looping combustion of methane, Chemical Engineering Journal 394 (2020) 124863. https://doi.org/10.1016/j.cej.2020.124863.

[16] Z. Cao, X. Zhu, K. Li, Y. Wei, F. He, H. Wang, Moderate-temperature chemical looping splitting of CO2 and H2O for syngas generation, Chemical Engineering Journal 397 (2020) 125393. https://doi.org/10.1016/j.cej.2020.125393.

[17] Y. Long, K. Li, Z. Gu, X. Zhu, Y. Wei, C. Lu, S. Lin, K. Yang, X. Cheng, D. Tian, F. He, H. Wang, Ce-Fe-Zr-O/MgO coated monolithic oxygen carriers for chemical looping reforming of methane to co-produce syngas and H2, Chemical Engineering Journal 388 (2020) 124190. https://doi.org/10.1016/j.cej.2020.124190.

[18] L. Li, Y. Song, B. Jiang, K. Wang, Q. Zhang, A novel oxygen carrier for chemical looping reforming: LaNiO3 perovskite supported on montmorillonite, Energy 131 (2017) 58–66. https://doi.org/10.1016/j.energy.2017.05.030.

[19] V.V. Galvita, H. Poelman, C. Detavernier, G.B. Marin, Catalyst-assisted chemical looping for CO2 conversion to CO, Applied Catalysis B: Environmental 164 (2015) 184–191. https://doi.org/10.1016/j.apcatb.2014.09.007.

[20] L.K. Rihko‐Struckmann, P. Datta, M. Wenzel, K. Sundmacher, Dharanipragada, N. V. R. A., H. Poelman, V.V. Galvita, G.B. Marin, Hydrogen and Carbon Monoxide Production by Chemical Looping over Iron‐Aluminium Oxides, Energy Technology 4 (2016) 304‑313. https://doi.org/10.1002/ente.201500231.

[21] J.M. Saad, P.T. Williams, Manipulating the H2/CO ratio from dry reforming of simulated mixed waste plastics by the addition of steam, Fuel Processing Technology 156 (2017) 331–338. https://doi.org/10.1016/j.fuproc.2016.09.016.

[22] L.C. Buelens, V.V. Galvita, H. Poelman, C. Detavernier, G.B. Marin, Super-dry reforming of methane intensifies CO2 utilization via Le Chatelier’s principle, Science 354 (2016) 449–452. https://doi.org/10.1126/science.aah7161.

[23] S.M. Sajjadi, M. Haghighi, Combustion vs. hybrid sol-gel-plasma surface design of coke-resistant Co-promoted Ni-spinel nanocatalyst used in combined reforming of CH4/CO2/O2 for hydrogen production, Chemical Engineering Journal 362 (2019) 767–782. https://doi.org/10.1016/j.cej.2019.01.085.

[24] S.A. Theofanidis, R. Batchu, V.V. Galvita, H. Poelman, G.B. Marin, Carbon gasification from Fe–Ni catalysts after methane dry reforming, Applied Catalysis B: Environmental 185 (2016) 42–55. https://doi.org/10.1016/j.apcatb.2015.12.006.

[25] F.-X. Chiron, G.S. Patience, S. Rifflart, Hydrogen production through chemical looping using NiO/NiAl2O4 as oxygen carrier, Chemical Engineering Science 66 (2011) 6324–6330. https://doi.org/10.1016/j.ces.2011.03.060.

[26] M. Rydén, A. Lyngfelt, T. Mattisson, Synthesis gas generation by chemical-looping reforming in a continuously operating laboratory reactor, Fuel 85 (2006) 1631–1641. https://doi.org/10.1016/j.fuel.2006.02.004.

[27] M. Rydén, A. Lyngfelt, T. Mattisson, Chemical-Looping Combustion and Chemical-Looping Reforming in a Circulating Fluidized-Bed Reactor Using Ni-Based Oxygen Carriers, Energy Fuels 22 (2008) 2585–2597. https://doi.org/10.1021/ef800065m.

[28] T. Pröll, J. Bolhàr-Nordenkampf, P. Kolbitsch, H. Hofbauer, Syngas and a separate nitrogen/argon stream via chemical looping reforming – A 140kW pilot plant study, Fuel 89 (2010) 1249–1256. https://doi.org/10.1016/j.fuel.2009.09.033.

[29] L.F. de Diego, M. Ortiz, J. Adánez, F. García-Labiano, A. Abad, P. Gayán, Synthesis gas generation by chemical-looping reforming in a batch fluidized bed reactor using Ni-based oxygen carriers, Chemical Engineering Journal 144 (2008) 289–298. https://doi.org/10.1016/j.cej.2008.06.004.

[30] L.F. de Diego, M. Ortiz, F. García-Labiano, J. Adánez, A. Abad, P. Gayán, Hydrogen production by chemical-looping reforming in a circulating fluidized bed reactor using Ni-based oxygen carriers, Journal of Power Sources 192 (2009) 27–34. https://doi.org/10.1016/j.jpowsour.2008.11.038.

[31] M. Ortiz, L.F. de Diego, A. Abad, F. García-Labiano, P. Gayán, J. Adánez, Hydrogen production by auto-thermal chemical-looping reforming in a pressurized fluidized bed reactor using Ni-based oxygen carriers, International Journal of Hydrogen Energy 35 (2010) 151–160. https://doi.org/10.1016/j.ijhydene.2009.10.068.

[32] M. Ortiz, A. Abad, L.F. de Diego, F. García-Labiano, P. Gayán, J. Adánez, Optimization of hydrogen production by Chemical-Looping auto-thermal Reforming working with Ni-based oxygen-carriers, International Journal of Hydrogen Energy 36 (2011) 9663–9672. https://doi.org/10.1016/j.ijhydene.2011.05.025.

[33] G. Diglio, P. Bareschino, R. Solimene, E. Mancusi, F. Pepe, P. Salatino, Numerical simulation of hydrogen production by chemical looping reforming in a dual fluidized bed reactor, Powder Technology 316 (2017) 614–627. https://doi.org/10.1016/j.powtec.2016.12.051.

[34] S. Wang, H. Lu, D. Li, Y. Tang, Simulation of the Chemical Looping Reforming Process in the Fuel Reactor with a Bubble-Based Energy Minimization Multiscale Model, Energy Fuels 27 (2013) 5008–5015. https://doi.org/10.1021/ef401101p.

[35] W.J. Hatcher, L. Viville, G.F. Froment, The Reoxidation of a Nickel Reforming Catalyst. Kinetic Analysis and Fixed Bed Simulation, Industrial & Engineering Chemistry Process Design and Development 17 (1978) 491–500. https://doi.org/10.1021/i260068a018.

[36] C. Linderholm, T. Mattisson, A. Lyngfelt, Long-term integrity testing of spray-dried particles in a 10-kW chemical-looping combustor using natural gas as fuel, Fuel 88 (2009) 2083–2096. https://doi.org/10.1016/j.fuel.2008.12.018.

[37] G.F. Froment, J. De Wilde, K.B. Bischoff, Chemical Reactor Analysis and Design, thirdrd ed., Wiley, Hoboken, N.J., 2010.

[38] Z. Zhou, L. Han, G.M. Bollas, Kinetics of NiO reduction by H2 and Ni oxidation at conditions relevant to chemical-looping combustion and reforming, International Journal of Hydrogen Energy 39 (2014) 8535–8556. https://doi.org/10.1016/j.ijhydene.2014.03.161.

[39] K. v. Manukyan, A.G. Avetisyan, C.E. Shuck, H.A. Chatilyan, S. Rouvimov, S.L. Kharatyan, A.S. Mukasyan, Nickel Oxide Reduction by Hydrogen: Kinetics and Structural Transformations, The Journal of Physical Chemistry C 119 (2015) 16131–16138. https://doi.org/10.1021/acs.jpcc.5b04313.

[40] J.A. Rodriguez, J.C. Hanson, A.I. Frenkel, J.Y. Kim, M. Pérez, Experimental and Theoretical Studies on the Reaction of H2 with NiO: Role of O Vacancies and Mechanism for Oxide Reduction, Journal of the American Chemical Society 124 (2002) 346–354. https://doi.org/10.1021/ja0121080.

[41] J.T. Richardson, R.M. Scates, M.V. Twigg, X-ray diffraction study of the hydrogen reduction of NiO/α-Al2O3 steam reforming catalysts, Applied Catalysis A: General 267 (2004) 35–46. https://doi.org/10.1016/j.apcata.2004.02.022.

[42] A. Abad, F. García-Labiano, L.F. de Diego, P. Gayán, J. Adánez, Reduction Kinetics of Cu-, Ni-, and Fe-Based Oxygen Carriers Using Syngas (CO + H2) for Chemical-Looping Combustion, Energy Fuels 21 (2007) 1843–1853. https://doi.org/10.1021/ef070025k.

[43] D. Ipsakis, E. Heracleous, L. Silvester, D.B. Bukur, A.A. Lemonidou, Reduction and oxidation kinetic modeling of NiO-based oxygen transfer materials, Chemical Engineering Journal 308 (2017) 840–852. https://doi.org/10.1016/j.cej.2016.09.114.

[44] C. Dueso, A. Abad, F. García-Labiano, L.F. de Diego, P. Gayán, J. Adánez, A. Lyngfelt, Reactivity of a NiO/Al2O3 oxygen carrier prepared by impregnation for chemical-looping combustion, Fuel 89 (2010) 3399–3409. https://doi.org/10.1016/j.fuel.2010.03.043.

[45] C. Dueso, M. Ortiz, A. Abad, F. García-Labiano, L.F. de Diego, P. Gayán, J. Adánez, Reduction and oxidation kinetics of nickel-based oxygen-carriers for chemical-looping combustion and chemical-looping reforming, Chemical Engineering Journal 188 (2012) 142–154. https://doi.org/10.1016/j.cej.2012.01.124.

[46] O. Dewaele, G.F. Froment, TAP Study of the Mechanism and Kinetics of the Adsorption and Combustion of Methane on Ni/Al2O3 and NiO/Al2O3, Journal of Catalysis 184 (1999) 499–513. https://doi.org/10.1006/jcat.1999.2473.

[47] R. Jin, Y. Chen, W. Li, W. Cui, Y. Ji, C. Yu, Y. Jiang, Mechanism for catalytic partial oxidation of methane to syngas over a Ni/Al2O3 catalyst, Applied Catalysis A: General 201 (2000) 71–80. https://doi.org/10.1016/S0926-860X(00)00424-5.

[48] E. Jerndal, T. Mattisson, A. Lyngfel, Thermal Analysis of Chemical-Looping Combustion, Chemical Engineering Research and Design 84 (2006) 795–806. https://doi.org/10.1205/cherd05020.

[49] M.C. Altay, S. Eroglu, Isothermal Reaction of NiO Powder with Undiluted CH4 at 1000 K to 1300 K (727 °C to 1027 °C), Metallurgical and Materials Transactions B 48 (2017) 2067–2076. https://doi.org/10.1007/s11663-017-0991-z.

[50] A. Abad, J. Adánez, F. García-Labiano, L.F. de Diego, P. Gayán, J. Celaya, Mapping of the range of operational conditions for Cu-, Fe-, and Ni-based oxygen carriers in chemical-looping combustion, Chemical Engineering Science 62 (2007) 533–549. https://doi.org/10.1016/j.ces.2006.09.019.

[51] J. Xu, G.F. Froment, Methane steam reforming, methanation and water-gas shift: I. Intrinsic kinetics, AIChE Journal 35 (1989) 88–96. https://doi.org/10.1002/aic.690350109.

[52] F.F. Tao, J.-J. Shan, L. Nguyen, Z. Wang, S. Zhang, L. Zhang, Z. Wu, W. Huang, S. Zeng, P. Hu, Understanding complete oxidation of methane on spinel oxides at a molecular level, Nat. Commun. 6 (2015) 7798. https://doi.org/10.1038/ncomms8798.

[53] K. Hou, R. Hughes, The kinetics of methane steam reforming over a Ni/α-Al2O catalyst, Chemical Engineering Journal 82 (2001) 311–328. https://doi.org/10.1016/S1385-8947(00)00367-3.

[54] S.-G. Wang, X.-Y. Liao, J. Hu, D.-B. Cao, Y.-W. Li, J. Wang, H. Jiao, Kinetic aspect of CO2 reforming of CH4 on Ni(111): A density functional theory calculation, Surface Science 601 (2007) 1271–1284. https://doi.org/10.1016/j.susc.2006.12.059.

[55] F. Minette, M. Lugo-Pimentel, D. Modroukas, A.W. Davis, R. Gill, M.J. Castaldi, J. De Wilde, Intrinsic kinetics of steam methane reforming on a thin, nanostructured and adherent Ni

coating, Applied Catalysis B: Environmental 238 (2018) 184–197. https://doi.org/10.1016/j.apcatb.2018.07.015.

[56] J.-W. Snoeck, G.F. Froment, M. Fowles, Kinetic Study of the Carbon Filament Formation by Methane Cracking on a Nickel Catalyst, Journal of Catalysis 169 (1997) 250–262. https://doi.org/10.1006/jcat.1997.1635.

[57] J.-W. Snoeck, G.F. Froment, M. Fowles, Steam/CO2 Reforming of Methane. Carbon Filament Formation by the Boudouard Reaction and Gasification by CO2 by H2 and by Steam: Kinetic Study, Industrial & Engineering Chemistry Research 41 (2002) 4252–4265. https://doi.org/10.1021/ie010666h.

[58] J.H. Park, R.H. Hwang, H.u. Rasheed, J.I. Baek, H.J. Ryu, K.B. Yi, Kinetics of the reduction and oxidation of Mg added NiO/Al2O3 for chemical looping combustion, Chemical Engineering Research and Design 141 (2019) 481–491. https://doi.org/10.1016/j.cherd.2018.11.021.

[59] D. Kunii, O. Levenspiel, Fluidization engineering, Elsevier, 1991.

[60] R.W. Breault, V.K. Mathur, High-velocity fluidized-bed hydrodynamic modeling. 1. Fundamental studies of pressure drop, Industrial & Engineering Chemistry Research 28 (1989) 684–688. https://doi.org/10.1021/ie00090a006.

[61] D. Kunii, O. Levenspiel, Fluidized reactor models. 1. For bubbling beds of fine, intermediate, and large particles. 2. For the lean phase: freeboard and fast fluidization, Industrial & Engineering Chemistry Research 29 (1990) 1226–1234.

[62] D. MEARS, Diagnostic criteria for heat transport limitations in fixed bed reactors, Journal of Catalysis 20 (1971) 127–131. https://doi.org/10.1016/0021-9517(71)90073-X.

[63] J.F. Davidson, D. Harrison, Fluidised particles, Cambridge, University Press, 1963.

[64] S.P. Sit, J.R. Grace, Interphase mass transfer in an aggregative fluidized bed, Chemical Engineering Science 33 (1978) 1115–1122. https://doi.org/10.1016/0009-2509(78)85017-9.

[65] F. Hernández-Jiménez, A. Gómez-García, D. Santana, A. Acosta-Iborra, Gas interchange between bubble and emulsion phases in a 2D fluidized bed as revealed by two-fluid model simulations, Chemical Engineering Journal 215-216 (2013) 479–490. https://doi.org/10.1016/j.cej.2012.10.056.

[66] J.A. Medrano, F. Gallucci, F. Boccia, N. Alfano, M. van Sint Annaland, Determination of the bubble-to-emulsion phase mass transfer coefficient in gas-solid fluidized beds using a non-invasive infra-red technique, Chemical Engineering Journal 325 (2017) 404–414. https://doi.org/10.1016/j.cej.2017.05.089.

[67] K. Miwa, I. Muchi, S. Mori, T. Kato, Behavior of bubbles in a gaseous fluidized-bed, International Chemical Engineering 12 (1972) 187-&.

[68] S. Mori, C.Y. Wen, Estimation of bubble diameter in gaseous fluidized beds, AIChE J. 21 (1975) 109–115. https://doi.org/10.1002/aic.690210114.

[69] M. Horio, A. Nonaka, A generalized bubble diameter correlation for gas-solid fluidized beds, AIChE J. 33 (1987) 1865–1872. https://doi.org/10.1002/aic.690331113.

[70] X. Li, A.J. Jaworski, X. Mao, Bubble size and bubble rise velocity estimation by means of electrical capacitance tomography within gas-solids fluidized beds, Measurement 117 (2018) 226–240. https://doi.org/10.1016/j.measurement.2017.12.017.

[71] J. Werther, Mathematische Modellierung von Wirbelschichtreaktoren, Chemie Ingenieur Technik 50 (1978) 850–860. https://doi.org/10.1002/cite.330501106.

[72] H.-m. Yan, C. Heidenreich, D.-k. Zhang, Mathematical modelling of a bubbling fluidised-bed coal gasifier and the significance of 'net flow', Fuel 77 (1998) 1067–1079. https://doi.org/10.1016/S0016-2361(98)00003-9.

[73] T. Pröll, P. Kolbitsch, J. Bolhàr - Nordenkampf, H. Hofbauer, A novel dual circulating fluidized bed system for chemical looping processes, AIChE Journal 55 (2009) 3255 - 3266. https://doi.org/10.1002/aic.11934.

[74] H.T. Bi, N. Ellis, I.A. Abba, J.R. Grace, A state-of-the-art review of gas–solid turbulent fluidization, Chemical Engineering Science 55 (2000) 4789–4825. https://doi.org/10.1016/S0009-2509(00)00107-X.

[75] M. Osman, A. Zaabout, S. Cloete, S. Amini, Internally circulating fluidized-bed reactor for syngas production using chemical looping reforming, Chemical Engineering Journal 377 (2019) 120076. https://doi.org/10.1016/j.cej.2018.10.013.

[76] Principal Features of UNS N06625. https://www.haynesintl.com/alloys/alloy-portfolio_/High-temperature-Alloys/HAYNES625Alloy/principal-features.aspx.

[77] C. Linderholm, M. Schmitz, A. Lyngfelt, Estimating the solids circulation rate in a 100-kW chemical looping combustor, Chemical Engineering Science 171 (2017) 351–359. https://doi.org/10.1016/j.ces.2017.05.025.

[78] X. Gao, T. Li, W.A. Rogers, K. Smith, K. Gaston, G. Wiggins, J.E. Parks, Validation and application of a multiphase CFD model for hydrodynamics, temperature field and RTD simulation in a pilot-scale biomass pyrolysis vapor phase upgrading reactor, Chemical Engineering Journal 388 (2020) 124279. https://doi.org/10.1016/j.cej.2020.124279.

[79] X.-B. Qi, J. Zhu, W.-X. Huang, A new correlation for predicting solids concentration in the fully developed zone of circulating fluidized bed risers, Powder Technology 188 (2008) 64–72. https://doi.org/10.1016/j.powtec.2008.03.012.

[80] M. Leva, Fluidization, McGraw-Hill, 1959.

[81] A.S. Gupta, G. Thodos, Direct analogy between mass and heat transfer to beds of spheres, AIChE J. 9 (1963) 751–754. https://doi.org/10.1002/aic.690090609.